

Focusing of magma in the upper mantle through dike interaction

Garrett Ito and Stephen J. Martel

Department of Geology and Geophysics, University of Hawaii at Manoa, Honolulu, Hawaii, USA

Received 30 March 2001; revised 16 March 2002; accepted 21 March 2002; published 11 October 2002.

[1] We use laboratory experiments and numerical models to quantify the effects of dike interaction on the focusing of magma as it ascends in the upper mantle. Laboratory experiments involve injecting buoyant fluid into the base of a tank filled with solidified gelatin. When we initiate two dikes parallel to each other, but separated by a horizontal distance x , they tend to merge as they ascend. This behavior is also predicted by numerical models of two-dimensional dikes. The key parameters that control the maximum horizontal separation x_c over which dikes will intersect are dike driving pressures, dike head lengths L (i.e., the length over which driving pressure is large), and the difference between the principal stresses of the remote stress field. When the remote differential stress is small compared to the dike driving pressure, two dikes of equal driving pressure and length will intersect over distances of $x_c \sim L$. This distance decreases with increasing remote differential stress. We quantify the effects on magma transport from a broad lateral distribution of magma using numerical simulations of multiple-dike interaction. When the average dike spacing prior to interaction is within $\sim 3L$ and remote differential stresses are insignificant, dike interaction can focus magma over horizontal distances many times L but at least $\sim 6L$. Dike interaction can focus magma in the asthenosphere beneath mid-ocean ridges for low mantle viscosities ($\leq 10^{19}$ Pa s) and if dikes initiate with average separations of a few hundred meters, or less. Such focusing is predicted to grow dikes of increasing magma flux approaching lateral separations of a kilometer. **INDEX TERMS:** 8434 Volcanology: Magma migration; 8145 Tectonophysics: Physics of magma and magma bodies; 3035 Marine Geology and Geophysics: Mid-ocean ridge processes; 8120 Tectonophysics: Dynamics of lithosphere and mantle—general; **KEYWORDS:** dike interaction, magma migration, fractures, mid-ocean ridge, laboratory experiment, lithosphere stress

Citation: Ito, G., and S. J. Martel, Focusing of magma in the upper mantle through dike interaction, *J. Geophys. Res.*, 107(B10), 2223, doi:10.1029/2001JB000251, 2002.

1. Introduction

[2] The transport and focusing of magma from the mantle to the Earth's surface is an important, yet poorly understood process. Focusing occurs over a range of scales. At the largest scale, magma focuses from broad melting zones in the mantle to individual storage zones in the crust and eruption sites at the surface. Previously explored mechanisms for focusing at this scale include pressure-driven intergranular flow [McKenzie, 1985; Phipps Morgan, 1987; Spiegelman and McKenzie, 1987; Scott and Stevenson, 1989], accumulation along lithospheric permeability boundaries [Sparks and Parmentier, 1991; Spiegelman, 1993], and accumulation of dikes due to local lithospheric stresses [Hieronymus and Bercovici, 2001; Muller et al., 2001]. At the smallest scale, magma concentrates from intergranular pores to high porosity channels. A possible mechanism for this scale of focusing is the reaction infiltration instability [Aharanov et al., 1995; Kelemen et al., 1995a, 1995b; Spiegelman et al., 2001]; a second possibility is localization of melt associated with matrix shear [Stevenson,

1989; Richardson, 1998; Zimmerman et al., 1999]. At mid-ocean ridges, this small scale of focusing is important in isolating melt from the bulk of the mantle during transport, thereby resulting in chemical disequilibrium between erupted magmas and the residual peridotite through which it passes [e.g., Salters and Hart, 1989; Johnson et al., 1990; Johnson and Dick, 1992].

[3] An intermediate scale of focusing involves the continued growth of melt channels and the growth of dikes. Geological observations at ophiolites indicate that porous flow channeling at mid-ocean ridges continues to the shallowest portions of the mantle [Kelemen et al., 1995a, 1995b, 1997]. In addition, dikes found in peridotites from mid-ocean ridges [Cannat, 1996; Dick and Natland, 1996] and ophiolites [Nicolas, 1990; Nicolas et al., 1994] indicate the importance of transport by hydraulic fracturing. Beneath mid-ocean ridges, the initiation of dikes may occur in the partial melting zone after some accumulation by porous flow [Nicolas, 1986, 1990]. Though the viscosity of the solid mantle is expected to be low, hydraulic fracturing is expected when dike fluid is several orders of magnitude less viscous than the host rock, a condition met by basaltic melts [Emerman and Marrett, 1990; Rubin, 1993a]. This intermediate scale of focusing is important not only in contri-

Table 1. Notation

Variable	Meaning	Value	Units
Δc	increment of dike growth		m
b	matrix grain size	10^{-3}	m
D	diffusivity of pore fluid pressure	4×10^{-3}	m ² /s
E	Young's Modulus		Pa
f	fraction of magma transported in dikes		
g	acceleration of gravity	9.8	m/s ²
G	mechanical energy release rate		J/m
h	length of dike head plus tail		m
k	matrix permeability		m ²
K_c	rock fracture toughness		Pa m ^{1/2}
K_I, K_{II}	mode I and mode II stress intensity factors at the upper tip		Pa m ^{1/2}
K_{IA}, K_{IB}	K_I for dike A and dike B		
L, L_A, L_B	dike head length		m
L_c	minimum vertical extent of a dike head in which $K_I = K_c$		m
\dot{M}	melt production rate in the mantle		s ⁻¹
n	initial number of dike heads		
P, P_0	variable and uniform dike driving pressure		Pa
$\bar{P}, \bar{P}_A, \bar{P}_B$	characteristic driving pressures		
\bar{Q}	magma flux		m ² s ⁻¹
\bar{Q}_0, \bar{Q}_f	average flux of starting dikes, average flux after dike interaction		m ² /s
r	radial distance		m
R_1, R_3	principle components of the remote stress field		Pa
ΔR	differential stress of the remote field ($R_1 - R_3$)		Pa
t, t_T	time, time for dike tail to thin to termination thickness		
U	ridge half spreading rate		m/s
U_E	mechanical energy release		J
V	dike propagation rate		m/s
V_D	magma flux per cross-sectional area		m/s
W	thickness of dike tail		
W_c	maximum thickness of a critical dike head in which $L = L_c$		m
W_T	termination thickness		m
u_n, u_s	normal and shear relative displacements of dike walls		m
x	horizontal distance from dike A		m
x_c	maximum separation distance that dike B merges with A		m
$\bar{x}, \bar{x}_0, \bar{x}_f$	average horizontal spacing, value prior to, and after dike interaction		m
X, Y	horizontal and vertical extent of arbitrary region in the mantle		m
y	height above base of the head of dike A		m
y_c	connection height on dike A		m
Δ	mean absolute misfit		
ϕ	porosity		
η, η_a	magma and asthenospheric viscosity	$10, 10^{19}$	Pa s
γ	fraction of net change in dike B's orientation θ_c^* defining average angle		
μ	shear Modulus		Pa
ν	Poisson's ratio		
Θ	angle from vertical axis beneath ridge axis		
θ_c	angle from vertical and the angle that maximizes G		
θ_c^*	angle from plane of dike B (when tip is at $y = 0$) to tip of dike A		
$\rho, \Delta\rho$	density, density contrast between ambient material and dike fluid		kg/m ³
σ_n, σ_s	normal and shear stress along dike		Pa

buting to melt-mantle disequilibrium, but also in producing melt volumes with sufficient dimension to penetrate the subsolidus lithosphere before freezing [Rubin, 1993b; Lister, 1994].

[4] While significant progress has been made in understanding the shape and propagation of individual dikes [e.g., Spence and Turcotte, 1985, 1990; Spence et al., 1987; Sleep, 1988; Lister, 1990; Lister and Kerr, 1991; Rubin, 1995], relatively little work has been done to examine how dikes accumulate magma and grow. One mechanism that has been studied is the influx of magma through the dike walls by porous flow [Sleep, 1988; Rubin, 1998]. A second mechanism is progressive coalescence due to dike interaction [Shaw, 1980; Takada, 1994a, 1994b]. Here, we address this second mechanism.

[5] We build upon the work of Takada [1994a, 1994b] by combining laboratory experiments with numerical models

to identify the controlling parameters of dike interaction. We first examine the interaction of two dikes and show that the results follow scaling laws derived from Griffith energy theory. Numerical models are then used to simulate the interaction of multiple dikes and quantify the length scales of magma focusing. Finally, we discuss the implications for magma transport in the upper mantle and crust of mid-ocean ridges.

2. Laboratory and Numerical Procedures and Observations

2.1. Laboratory Experimental Procedure

[6] The first, most simple interaction to study is between two dikes in a linear elastic solid subject to an isotropic remote stress field. This is done with laboratory experiments that involve injecting buoyant fluid into solidified gelatin.

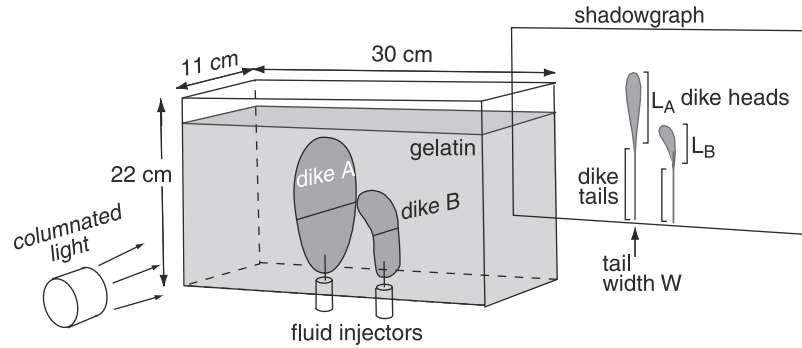


Figure 1. Schematic illustration of laboratory experimental apparatus. Fluid was injected through the base of a tank filled with solidified gelatin solution to form synthetic dikes. Dikes were imaged by projecting columnated light through the gelatin and onto a projection screen. Buoyant fluid forms tear-drop shaped dike “head” in cross section, trailed by a thin dike “tail”.

[7] Gelatin has been used to address a variety of issues in dike mechanics including the shape and propagation rate of buoyant dikes [Takada, 1990; Heimpel and Olson, 1994], effects of local geologic stresses on dike propagation [Fiske and Jackson, 1972; Muller et al., 2001], and dike interaction [Takada, 1994a, 1994b]. Gelatin is a weak elastic and transparent solid, and therefore dikes are easy to grow and observe. We used 250A ordnance grade gelatin from the Kind and Knox Company. The gelatin was dissolved in hot water at a concentration of 1.5% by weight and then solidified at a temperature of 4°C. We estimate the shear modulus μ (see Table 1 for definition of variables) of this concentration to be 444 ± 88 Pa based on comparisons of dike aspect ratios in the laboratory with those predicted by analytic solutions of static, buoyant cracks [Sneddon, 1946; Heimpel and Olson, 1994]. The Poisson’s ratio ν of the gelatin is ~ 0.5 and the density is very close to that of water, $\rho = 1.0 \times 10^3$ kg/m³.

[8] The fluid used to fill one dike (dike A) is hexane (Figure 1). This yielded a buoyant dike with a low-density

contrast with the gelatin ($\Delta\rho = 336$ kg/m³) and a low ascent speed of $\sim 10^{-4}$ m/s. The fluid used for the second dike (dike B) was air. Air dikes were much more buoyant and rose much faster (10^{-3} – 10^{-2} m/s) than the hexane dikes. Though the use of two fluids of different densities differs from two magma-filled dikes of the same density, the slow hexane dikes allowed us enough time to photograph the experiments, while the small and faster air-filled dike B minimized the required tank volume and experimental duration. We will quantify the effects of fluid density differences on dike interaction in our scaling analyses that follow.

[9] We began each experiment by first injecting dike A (hexane) through a silicon-sealed hole at the base of the tank. We set the initial orientation to be vertical by cutting the gelatin with the injection needle. As dike A rose, it preserved a “head” that is tear-drop shaped in cross section. The rising head left behind a thin “tail” where the walls are nearly closed. In the experiments, the base of the head is identified as where the dike head appears to

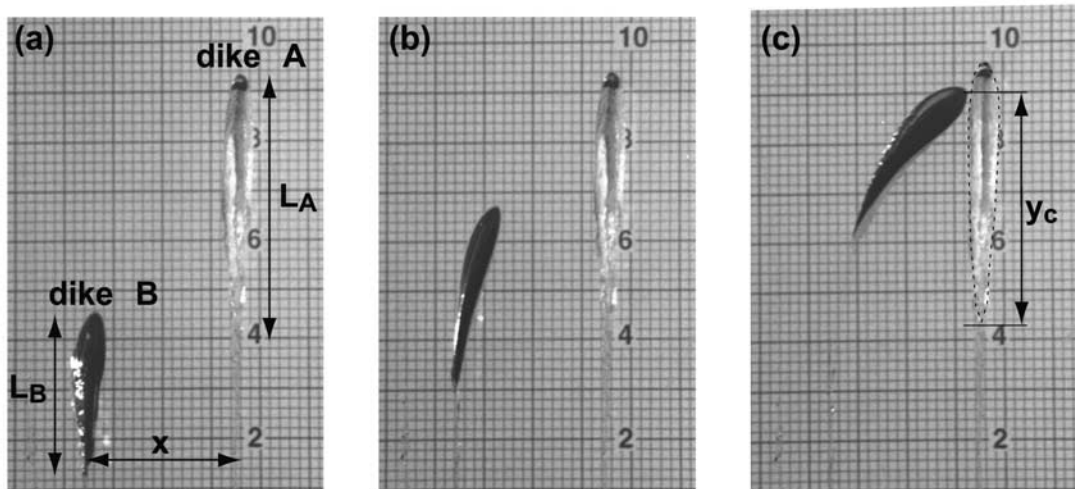


Figure 2. Time series of photographs illustrating how dike B (air) interacts with dike A (hexane). Dike tails are very thin so only dike heads are visible. (a) Both dikes are initiated parallel to each other. (b) As dike B ascends, it begins to curve toward dike A. (c) Dike B intersects dike A at a height y_c measured above the base of dike A. The head of dike A is outlined for clarity. See color version of this figure at back of this issue.

pinch out (Figures 1 and 2). The head size remains nearly constant and the tail lengthens to accommodate ascent of the head. After the bottom of dike A's head rose at least 0.03–0.035 m above the base of the tank we injected dike B. We aligned dike B parallel to dike A and offset it by a lateral distance x . As dike B rose, it also formed a tear-drop shaped head, trailed by a very thin and lengthening tail. Dike B first propagated vertically but as its upper tip approached the level of the base of dike A's head, dike B began to curve toward dike A and, if sufficiently close, it intersected dike A (Figure 2). Using a shadowgraph image of the tank we measured the head lengths of dike A (L_A) and dike B (L_B) as well as the height of intersection (y_c , measured above the base of dike A's head).

[10] To test the importance of the tank boundaries, the free surface of the gelatin, dike aspect ratio, and possible anisotropy in the gelatin prior to dike injection, we injected a single air-filled dike at different inclinations. Regardless of the inclination, the dike propagated nearly in-plane, or at least did not curve in a systematic fashion. These tests confirmed that dike interaction was the dominant influence on dike trajectories.

2.2. Dike Shape and Propagation in the Laboratory and in the Earth

[11] The shape and propagation rate of a dike driven by magma buoyancy are controlled by fluid flow of magma, fracture mechanics, and elasticity of the host rock [Spence *et al.*, 1987; Lister, 1990; Spence and Turcotte, 1990; Lister and Kerr, 1991; Rubin, 1995]. Tip effects near the top of the dike result in the characteristic tear-drop shaped dike head. The effects of the upper tip decay with distance from the tip and are negligible in the narrow portion of the dike, which we refer to as the dike tail. Dike walls separate because the fluid pressure in the dike exceeds the remote compressive stress normal to the dike. This excess pressure is called the driving pressure. Driving pressure is greatest near the upper tip of the head, negative near the base of the head, and near zero in the tail [Spence *et al.*, 1987; Lister, 1990; Rubin, 1998]. Dike interaction is controlled mostly by the stress perturbations around the dike head, and therefore, we discuss the factors that control the head size and driving pressures in the laboratory versus in the Earth.

[12] The stresses near the tip of a fracture control whether it can propagate and the direction in which it might propagate. According to principles of linear elastic fracture mechanics, the stresses (σ_{ij}) near the tip of an opening-mode (i.e., mode I) fracture are of the form [e.g., Lawn, 1993]

$$\sigma_{ij} = \frac{K_I}{\sqrt{2\pi r}} f_{ij}(\theta), \quad (1)$$

where K_I is a constant known as the mode I stress intensity factor, r is the distance from the fracture tip, and θ is the angular position about the fracture tip. The stress intensity factor is a function of the fracture geometry and the driving pressure distribution [Tada *et al.*, 1985]. The value of K_I at the upper tip is most sensitive to the length and driving pressure associated with the dike head rather than the dike tail.

[13] For the fluid volumes used in our laboratory experiments, K_I for the upper tip remains below the fracture

toughness K_c of the gelatin. This subcritical propagation results in an ascent rate V that is a power law function of K_I [Heimpel and Olson, 1994]. The rate that the dike fluid rises is governed by laminar flow through a slot [Turcotte and Schubert, 1982] and therefore

$$V = \frac{\Delta\rho g}{12\eta} W^2. \quad (2)$$

Here, W is the thickness of the tail, $\Delta\rho$ is the density contrast between the dike fluid and ambient material, g is gravitational acceleration, and η is magma viscosity (also see Table 1). Subcritical ascent is slow and therefore the tail is very thin and the vertical pressure gradient dP/dy in the dike head remains very close to hydrostatic (i.e., $dP/dy = \Delta\rho g$).

[14] In contrast, dikes in the Earth are considered to propagate with a stress intensity factor at the upper tip equal to the fracture toughness (i.e., $K_I = K_c$). Under this condition, the rate of dike ascent is not controlled by K_I but rather the viscosity of magma in the dike tail [Spence *et al.*, 1987; Lister, 1990; Spence and Turcotte, 1990]. For a dike on the verge of propagating, the head has a minimum length of $L = L_c$ [Weertman, 1971; Secor and Pollard, 1975], and there is no tail. Only for this critical dike is the driving pressure in the head precisely hydrostatic. Larger dikes will ascend more rapidly and have wider tails, head lengths greater than L_c , and a pressure gradient (dP/dy) less than hydrostatic [Spence *et al.*, 1987; Lister, 1990; Spence and Turcotte, 1990; Rubin, 1998].

[15] To account for the above differences between laboratory and natural dikes as well as to allow for applicability to a range of dike sizes in the Earth, it will be important to appropriately scale the lengths and pressure-gradients associated with dike heads. Also, even though a fixed volume of fluid is injected to form dikes in the laboratory, the ascent rate and size of the dike head remains nearly constant as the dikes ascend. The reason for this behavior is that the tail is much thinner than the head and therefore lengthening of the tail over the laboratory domain removes very little fluid from the head. (Also, the total decompression of the rising dikes is small compared atmospheric pressure and therefore decompression changes dike volumes insignificantly.) In contrast in the Earth, tail volume can be large compared to that of the head and therefore dike ascent can lead to a decrease in propagation rate and head size for dikes of constant volume. A constant ascent rate and head size will occur in the Earth, however, when the tail is fed from below by a constant magma flux. In this sense, our laboratory experiments best simulate magma-filled dikes of constant tail flux.

2.3. Numerical Method

[16] We use two-dimensional (2-D, plane strain) numerical models to simulate the laboratory experiments as well as to examine a larger range of parameters than are possible in the laboratory. To calculate the stress field and propagation of the two dikes, we used a modified version of the boundary element code TWODD [Crouch and Starfield, 1983]. This method has proven efficient in modeling the propagation of fractures [Olson and Pollard, 1989, 1991; Roering *et al.*, 1997; Muller and Martel, 2000]. The method

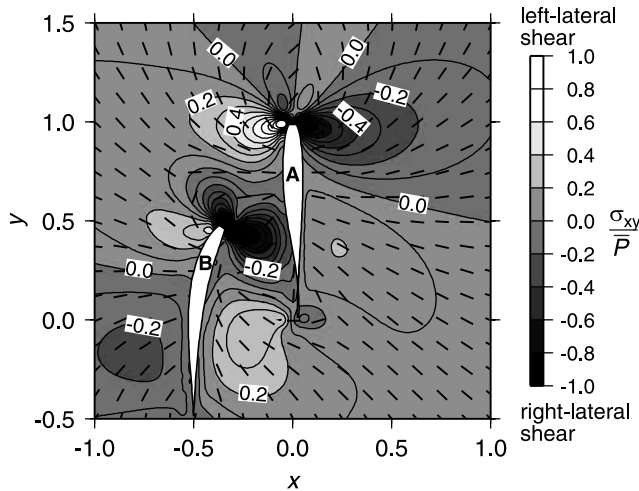


Figure 3. Shear stresses (σ_{xy} normalized by the average driving pressure \bar{P}) predicted by a 2-D numerical model of two dikes of equal buoyancy and length. Stresses are contoured at intervals of 0.2 and shaded, and computed dike shape is white. On a vertically oriented plane, positive shear (light shading) is left lateral and negative shear (dark shading) is right lateral. Ticks show trajectories of minimum principle tensile stress. This figure and those that follow were generated using GMT [Wessel and Smith, 1995].

uses a Green's function formulation by dividing cracks into discrete elements along which boundary stresses are defined. For each boundary element, analytic solutions of the equilibrium and compatibility equations predict stresses and displacements in the elastic material surrounding the cracks. The contributions from all elements are summed to give the total stress and displacement field perturbations due to both dikes.

[17] The slow rise of laboratory dikes results in a driving pressure distribution P in the dike head much like that of a stationary dike [Secor and Pollard, 1975],

$$P = (dP/dy)(y - L/4) + P_0, \quad (3)$$

where y is height above the base of the dike head, $dP/dy = \Delta\rho g$, g is gravitational acceleration, and $\Delta\rho$ is the density contrast between the dike fluid and ambient material (also see Table 1). Dike head length L is kept constant within each calculation, which simulates our laboratory experiments as well as magma-filled dikes fed by a constant flux. For buoyant dikes, we set $P_0 = 0$ [Secor and Pollard, 1975] at the start of the calculations when the dikes were far apart, but as the dikes began to interact, we iteratively solved for P_0 such that dike head volume remained constant. We define a characteristic driving pressure as $\bar{P} = (dP/dy)L/2$, which for the laboratory is $\Delta\rho gL/2$. We also maintained zero shear traction along the dike head throughout the calculations. For simplicity, driving stresses are only specified along the dike head, and therefore the tail behaves just as the surrounding unfractured rock. On dike B, this condition minimizes the relative shear displacement across the tail (induced by dike A) and thus leads to an underprediction in the degree to which dike A bends dike B's trajectory. The effects of the tail on dike trajectory,

however, is likely to be of second-order importance as shown by comparing calculations without tails to those with tails that support zero shear [Muller et al., 2001].

[18] Crack propagation was calculated by first computing the stresses near (within a distance of $0.025L$) the tip of the dike head. We then determined the orientation of the next growth increment that minimized the shear stress along the new increment [Anderson, 1936; Olson and Pollard, 1991]. The tip element of the dike was then moved upward into this orientation, and the elements below were shifted up the dike by $0.025L$. To optimize numerical accuracy and efficiency, we defined the elements to be shortest ($0.025L$) near the upper tip and to lengthen toward the base of the dike head where they reached a maximum of $0.05L$. Laboratory experimental conditions were simulated by initiating the heads of dike A and B vertically, with dike B injected a distance x to the side of dike A, and a distance $0.5L_A$ below it. Dike A remained stationary and dike B propagated upward.

2.4. Mechanics of Dike Interaction and Scaling Parameters

[19] Both the laboratory experiments and numerical models showed a tendency for dike B to curve toward dike A. Calculations of shear stress, σ_{xy} (x and y are horizontal and vertical coordinates, respectively, with the origin fixed at the rising base of the head dike A), surrounding the two dikes reveal how dike B is steered (Figure 3). In the absence of dike B, σ_{xy} is antisymmetric about dike A; in Figure 3, an approximately antisymmetric field exists for $y/L_A > 0.75$. The region encompassing dike B is dominated by negative shear, therefore the vertically oriented dike experiences right-lateral shear and curves to the right. This behavior can also be understood in terms of stress trajectories [Takada, 1994a, 1994b]. Dikes tend to open in the direction of maximum tension and propagate parallel to the direction of minimum tension. The opening of dike A directs trajectories of minimum tension toward it and thus causes the curving of dike B toward dike A.

[20] Analytic solutions predict stress perturbations of an isolated crack to depend on the distance away from the crack and increase with crack driving pressure and length [Pollard and Segall, 1987]. We thus anticipate that the fundamental parameters controlling dike interaction are \bar{P} , L , as well as the relative positions of two dikes.

2.5. Intersection Height and Dike Separation

[21] Here we quantify the effects of dike driving pressure, length, and separation distance x on the connection height y_c above base of the head of dike A at the time of intersection (see Figure 2). To generalize our results we scale all lengths by the length L_A of dike A and scale the pressures by the characteristic driving pressure of dike A, $\bar{P}_A = (dP/dy_A)L_A/2$.

Table 2. Laboratory Experimental Parameters

Case	Dike A (Hexane) Volume, mL	Dike B (Air) Volume, mL	Average Lengths, 10^{-2} m	
			Dike B	Dike A
a	5.0	1.5	2.74	5.32
b	5.0	2.2	3.24	5.51
c	5.0	3.0	3.71	5.37
d	3.0	8.0	4.04	4.21

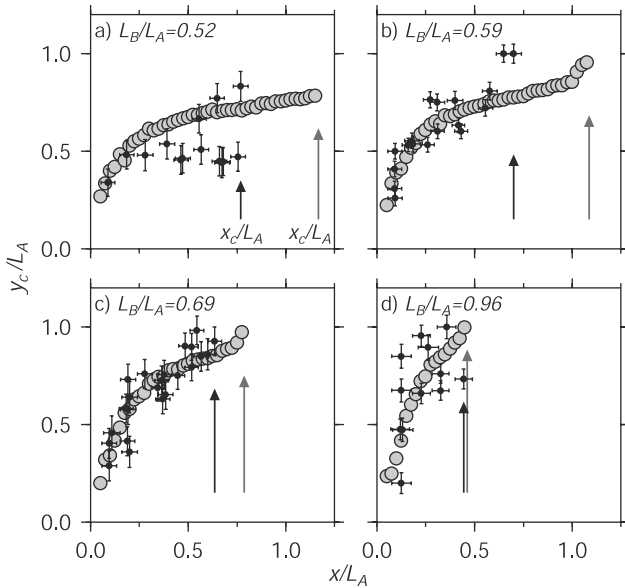


Figure 4. The height y_c of connection is normalized by the length of dike A, L_A , and plotted as a function of normalized separation distance x_c/L_A for different ratios of dike lengths L_B/L_A . Box letters correspond to the four cases listed in Table 2. Gray circles are results of 2-D numerical models, and black symbols are results of 3-D laboratory experiments. Error bars reflect measurement uncertainties. Arrows mark the maximum distance that intersections occur in models (gray) and experiments (black).

We then vary the dimensionless driving pressure $\bar{P}_B/\bar{P}_A = (dP/dy_B L_B)/(dP/dy_A L_A)$ and length L_B/L_A of dike B. In the laboratory, these two parameters were varied together by injecting different volumes of air and hexane (Table 2); however, in numerical models we varied \bar{P}_B/\bar{P}_A independent of L_B/L_A by changing the pressure gradient ratio $(dP/dy_B)/(dP/dy_A)$. Also, as pressure-gradient can vary in the Earth depending on the flux conditions feeding each dike, varying $(dP/dy_B)/(dP/dy_A)$ allows us to quantify its effects on dike interaction.

[22] Figure 4 illustrates the dependence of connection height on initial separation distance for four sets of laboratory experiments with $L_B/L_A = 0.52-0.96$ and $\bar{P}_B/\bar{P}_A = 1.55-2.86$ (Table 2). The normalized intersection height y_c/L_A increases with separation distance to a maximum normalized distance x_c/L_A , beyond which dike B fails to curve enough to connect. There is some scatter in y_c/L_A at a given separation distance due to imperfections in the experimental technique and conditions. For example, Figure 4a ($L_B/L_A = 0.52$) shows the largest scatter in y_c/L_A because the speed of the two dikes became comparable, thus making y_c/L_A highly sensitive to subtle perturbations to dike B's propagation path (dike B was effectively hitting a moving target). Connection heights predicted by the numerical models are consistent with laboratory values over a broad range of x/L_A . The major difference between the models and experiments are that the 2-D models predict connections over greater normalized separations x_c/L_A than laboratory dikes, particularly for the lowest values of L_B/L_A . This difference is most likely due

to 3-D effects in the laboratory not simulated in the 2-D numerical models (the laboratory dikes are of finite dimension normal to the plane of Figure 2) and is therefore important to quantify.

3. Parameterization of Maximum Distance of Dike Connection

[23] The purpose of this analysis is to develop scaling laws that describe the dependence of maximum normalized connection distance x_c/L_A on the parameters \bar{P}_B/\bar{P}_A and L_B/L_A . We will show that the behavior of two interacting dikes can be parameterized according to energy concepts [Griffith, 1920, 1924] which describe the propagation of a single crack subject to opening (mode I) and shear (mode II) driving stresses.

3.1. Dependence on Driving Pressure

[24] Using numerical models, we compute the maximum normalized connection distance x_c/L_A for different values of \bar{P}_A/\bar{P}_B while keeping $L_A/L_B = 1.0$. The first set of calculations involves dike heads with a uniform driving pressure, $\bar{P} = P_0$ and a range of pressure ratios ($\bar{P}_A/\bar{P}_B = 0.2-2.0$). These calculations are not meant to simulate realistic conditions in the Earth, rather they are only meant to reveal the basic mechanics. The second set of calculations involve buoyant dike heads with $\bar{P}_A/\bar{P}_B = (dP/dy_A)/(dP/dy_B)$ spanning a range 0.33–1.0.

[25] Figure 5a illustrates the increase in x_c/L_A with \bar{P}_A/\bar{P}_B . The constant-pressure calculations are well fit by the scaling law,

$$x_c/L_A = 1.33(\bar{P}_A/\bar{P}_B)^{0.70 \pm 0.06} \quad (4)$$

with a mean absolute misfit $\Delta = 0.02$. The uncertainty in the exponential term is defined such that Δ is within a factor of two of the minimum misfit. Calculations of buoyant dikes are fit by the scaling law

$$x_c/L_A = 1.22(\bar{P}_A/\bar{P}_B)^{0.87 \pm 0.10} \quad (5)$$

($\Delta = 0.05$). The similarity of equations (4) and (5) (Figure 5a) indicates that for constant-pressure versus buoyant dikes, the average driving pressure is more important for evaluating the gross interaction of the dikes rather than precise differences in driving pressure distribution.

[26] The cause of the above scaling laws can be addressed by considering basic theory of mixed-mode fracture propagation. As introduced by Griffith [1920, 1924], the mechanical energy released ΔU_E upon lengthening of a single crack (i.e., dike B) by an infinitesimal amount Δc is

$$\Delta U_E = \int_{\Delta c}^0 (\sigma_n u_n + \sigma_s u_s) dr, \quad (6)$$

where σ_n and σ_s are the normal and shear components of stress at a (small) radial distance r from the tip of the crack, and u_n and u_s are the corresponding components of virtual displacement that would occur after the crack lengthens by Δc (Figure 5b). Stresses and displacements immediately in

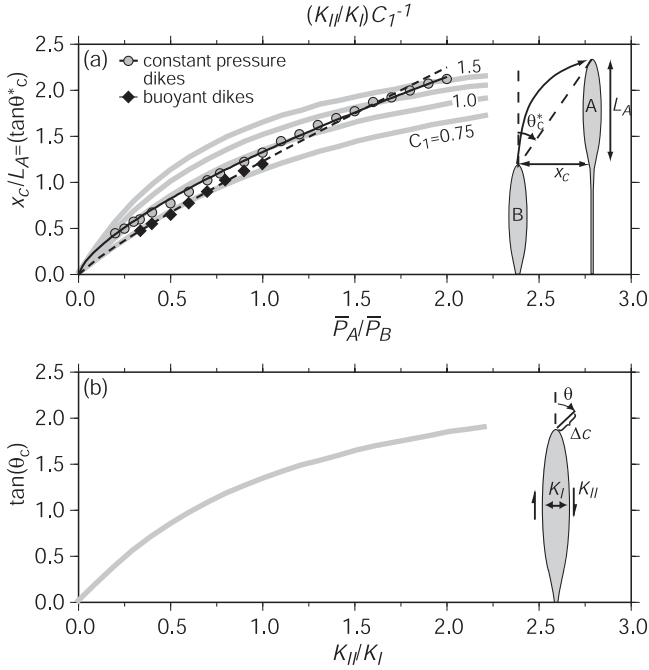


Figure 5. (a) Dependence of maximum connection distance x_c normalized by dike head length L_A on the ratio of characteristic dike pressures, predicted by numerical models of two interacting dikes. Circles show results of constant-pressure dikes and solid diamonds show results of buoyant dikes. Best fitting curves are shown for constant-pressure dikes (solid, equation (4)) and buoyant dikes (dashed, equation (5)) with respective root-mean-square misfits of 0.023 and 0.025. Inset illustrates geometry and definition of variables. Gray curves show predictions from equations (6)–(9) for different values of C_1 . (b) Predictions of Griffith's energy theory. The tangent of the angle θ (see inset) that maximizes the mechanical energy release rate upon lengthening of a dike increases with the ratio of the mode II to mode I stress intensity factor K_{II}/K_I .

front of the tip of a crack are proportional to stress intensity factors (e.g., equation (1)). In the opening mode (mode I), the stress intensity factor K_I at the upper tip is

$$K_I = C\bar{P}(L/2)^{1/2}, \quad (7)$$

where C is a constant that reflects the crack geometry. For a crack of uniform driving pressure, the characteristic driving pressure $\bar{P} = P_0$ and $dP/dy = 0$ in (3). For a buoyant crack, $\bar{P} = (dP/dy)L/2$ and $P_0 = 0$. For a 2-D planar crack $C = \pi^{1/2}$ [Tada et al., 1985; Lawn, 1993]. For a penny-shaped (3-D) crack, $C = 2\pi^{-1/2}$ in the case of uniform driving pressure. The shear mode (mode II) stress intensity factor at the upper tip K_{II} has the same form as equation (7), but with a characteristic driving shear stress replacing \bar{P} .

[27] To derive an equation for the rate of mechanical energy release dU_E/dc in 2-D, Lawn [1993] evaluated the integral in equation (6) using analytic solutions of near-tip stresses and displacements. After taking the limit as $\Delta c \rightarrow 0$, Lawn [1993] showed that the rate of mechanical energy

release depends on K_I , K_{II} , and the angle θ with respect to the crack plane according to

$$\frac{dU_E}{dc} = \frac{(1 - \nu^2)}{E} [K_I'(\theta)^2 + K_{II}'(\theta)^2] \equiv G(\theta). \quad (8)$$

The primes denote “effective” stress intensity factors defined as

$$K_I'(\theta) = [K_I F_{\theta 0}^I + K_{II} F_{\theta 0}^{II} (2\pi r)^{1/2}] \text{ and } K_{II}'(\theta) = [K_I F_{\theta 0}^I + K_{II} F_{\theta 0}^{II}]. \quad (9)$$

The four functions F are associated with two stress components in polar coordinates (double subscripts) arising from each mode of loading (superscripts). Assuming the crack will propagate in the direction of angle θ_c that maximizes $G(\theta)$, equations (8) and (9) predict that θ_c will increase with K_{II}/K_I (Figure 5b). This prediction is consistent with predictions of Takada [1994a].

[28] We now parameterize the interaction of two dikes based on the above theory. The first quantity that relates numerical model results to Griffith's theory of a single crack subject to mixed-mode driving stresses is the ratio x_c/L_A . This ratio is the tangent of the angle θ_c^* between vertical and a line drawn from the initial tip of dike B to the tip of dike A (Figure 5a). One can think of θ_c^* as a net change in dike B's orientation after it propagates from its starting position to the point at which it just intersects dike A. Thus θ_c^* is a measure of the change in the orientation of dike B much like θ_c is a measure of the change in orientation of a single crack subject to mixed mode stresses.

[29] The second quantity relating dike interaction to Griffith's crack theory is the pressure ratio \bar{P}_A/\bar{P}_B . The opening of dike A induces shear stress along the surface of dike B. The mode II stress intensity factor at the upper tip of dike B is thus proportional \bar{P}_A , whereas the mode I stress intensity factor at the upper tip of dike B depends primarily on \bar{P}_B . The ratio \bar{P}_A/\bar{P}_B should therefore control K_{II}/K_I at the upper tip of dike B. We anticipate that there is a ratio of stress-intensity factors at the upper tip of dike B, $(K_{II}/K_I)^*$ that represents an average over dike B's whole trajectory. This average can be described by

$$(K_{II}/K_I)^* = C_1 F(L_A/L_B) \frac{\bar{P}_A}{\bar{P}_B}. \quad (10)$$

Here, C_1 is a constant and F is an unspecified function of L_A/L_B , which we define to be unity when $L_A/L_B = 1$. Equation (10) adequately describes an average stress intensity factor ratio for dike B if it predicts a change in $\tan(\theta_c^*)$ much like K_{II}/K_I changes $\tan(\theta_c)$.

[30] One way to compare our numerical model results with the predictions of Griffith's crack theory, would be to plot $\tan(\theta_c^*)$ versus $(K_{II}/K_I)^*$ (i.e., the numerical results) with the theoretical curve in Figure 5b. But instead for clarity, we plot $\tan(\theta_c)$ versus $(K_{II}/K_I)/C_1$ (i.e., curve predicted by Griffith's theory) with the numerical results in Figure 5a. The constant-pressure and buoyant dike results are bounded by curves for $C_1 = 0.8$ and 1.2. A constant value of $C_1 = 1.0$ yields a root-mean square misfit to both sets of numerical results of only 7–15% of the maximum values of x_c/L_A . With $C_1 = 1.0$ and $F = 1.0$ (as defined for

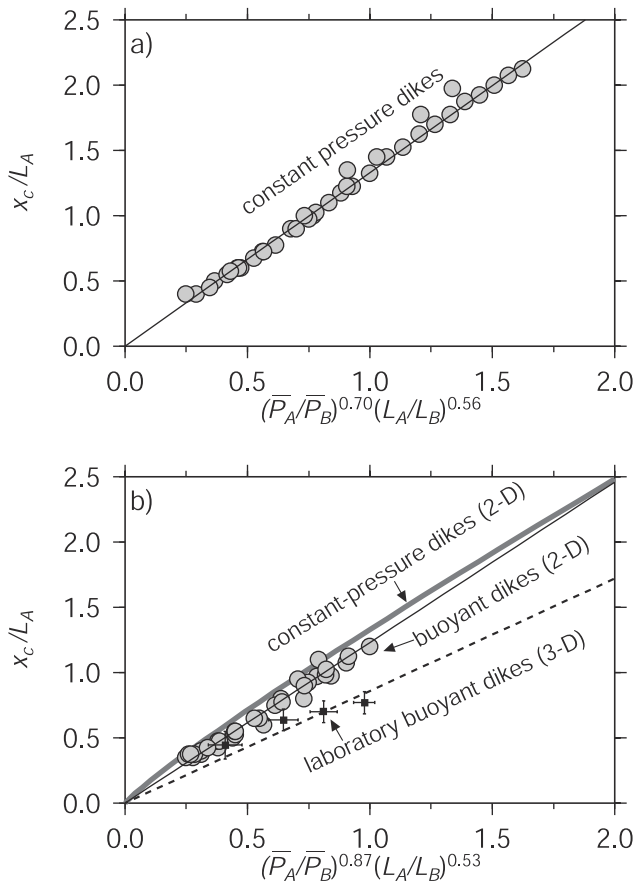


Figure 6. Normalized maximum distance that two dikes intersect is a function of pressure and length ratios, \bar{P}_A/\bar{P}_B and L_A/L_B . (a) Numerical results of constant pressure dikes are best fit by the solid line given by equation (11). (b) Numerical results of buoyant dikes (gray circles) are fit by solid curve (equation (12)) and results of laboratory dikes (black symbols) are fit by dashed curve (equation (13)). The best fitting function for constant-pressure dikes is also plotted for reference (gray).

$L_A/L_B = 1.0$), equations (4) and (10) suggest that $x_c/L_A = 1.33(K_{II}/K_I)^{0.70}$. Likewise, equations (5) and (10) suggest $x_c/L_A = 1.22(K_{II}/K_I)^{0.87}$. Thus if dike B slightly trails a neighboring dike A, then increasing the pressure ratio \bar{P}_A/\bar{P}_B , on average, increases K_{II}/K_I at the upper tip of dike B. This essentially moves dike B up the curve predicted by Griffith's crack theory (Figure 5b) and dike B turns more sharply to dike A.

3.2. Dependence on Dike Length

[31] Here we examine the dependence of maximum connection distance on the length ratio L_A/L_B . For the same values of \bar{P}_A/\bar{P}_B examined above, we vary the length ratio L_A/L_B of two interacting dikes and determine x_c/L_A from numerical model calculations. In constant-pressure calculations, L_A/L_B is varied from 0.083 to 4.0. In buoyant-dike calculations, L_A/L_B is varied from 0.37 to 1.67, subject to the constraint that $K_{IB}/K_{IA} \geq 1.0$ in order for dike B to rise faster than dike A [Heimpel and Olson, 1994]. Figure 6 shows results of 38 calculations for constant pressure dikes, and 33 for buoyant dikes. Normalized maximum connection

distance is plotted versus our best fitting function of the pressure and length ratios. The closeness of fit is reflected in the degree to which the results fall along a single line. The best fitting function for the constant-pressure dike calculations is

$$x_c/L_A = 1.33(\bar{P}_A/\bar{P}_B)^{0.70 \pm 0.06}(L_A/L_B)^{0.56 \pm 0.10}, \quad (11)$$

with $\Delta = 0.04$, and the best fitting function for the buoyant dike calculations is

$$x_c/L_A = 1.22(\bar{P}_A/\bar{P}_B)^{0.87 \pm 0.10}(L_A/L_B)^{0.53 \pm 0.28}, \quad (12)$$

with $\Delta = 0.05$. The above results can be used to estimate the function F in equation (10). We equate the right-hand side of equation (11) to $1.33(K_{II}/K_I)^{0.70}$ and the right-hand side of equation (12) to $1.22(K_{II}/K_I)^{0.87}$. The function F is therefore approximately $(L_A/L_B)^{0.56/0.70} = (L_A/L_B)^{0.8}$ for constant-pressure dikes and approximately $(L_A/L_B)^{0.53/0.87} = (L_A/L_B)^{0.61}$ for buoyant dikes.

[32] We now plot the results of the 3-D laboratory dikes with the same scaling derived for the numerical calculations of buoyant dikes (Figure 6b). The best fitting function is

$$x_c/L_A = 0.86(\bar{P}_A/\bar{P}_B)^{0.87}(L_A/L_B)^{0.53}. \quad (13)$$

The smaller coefficient of 0.86 compared to 1.22 for numerical buoyant dikes indicates that, for the same value of $(\bar{P}_A/\bar{P}_B)^{0.87}(L_A/L_B)^{0.53}$, the laboratory dikes intersect at a shorter maximum normalized separation distances (x_c/L_A). Figure 4 shows this result too. With the constraint of $K_{IB}/K_{IA} \geq 1.0$ for buoyant dikes, the normalized connection distance is maximized when $K_{IB}/K_{IA} = 1$ (i.e., $\bar{P}_A/\bar{P}_B = L_A/L_B = 1.0$). For 2-D buoyant dikes, the maximum connection distance is $1.2L_A$ (Figure 6b). For 3-D laboratory dikes, the maximum connection distance is $\sim 0.77L_A$, or roughly 0.64 times the maximum connection distance predicted for 2-D dikes. This reducing factor most likely results from the difference between 2-D and 3-D geometries. The magnitude of the shear stress perturbation associated with a penny-shaped (3-D) crack [Sneddon, 1946] decays more rapidly with distance than that of a 2-D crack [Pollard and Segall, 1987]. Shear stress perturbations around a penny-shaped dike A will therefore attract dike B toward it over shorter distances than if the dikes were two dimensional.

4. Effects of Remote Stresses

[33] So far, we have considered interaction of dikes when differential remote stresses are negligible compared to the dike driving pressures. Here we use numerical models and Griffith theory to quantify the effects of remote differential stress that are comparable to dike driving pressures.

[34] In these models, we vary the remote differential stress around two dikes with $\bar{P}_A/\bar{P}_B = L_A/L_B = 1.0$. We set the most tensile remote stress R_1 to be horizontal (perpendicular to initial dike planes) and the least principal tensile stress R_3 to be vertical (parallel to initial dike planes) (Figure 7a). The remote differential stress $\Delta R = (R_1 - R_3)$ is varied by keeping R_1 constant and changing R_3 . The characteristic driving pressure \bar{P} ($= \bar{P}_A = \bar{P}_B$) is defined as

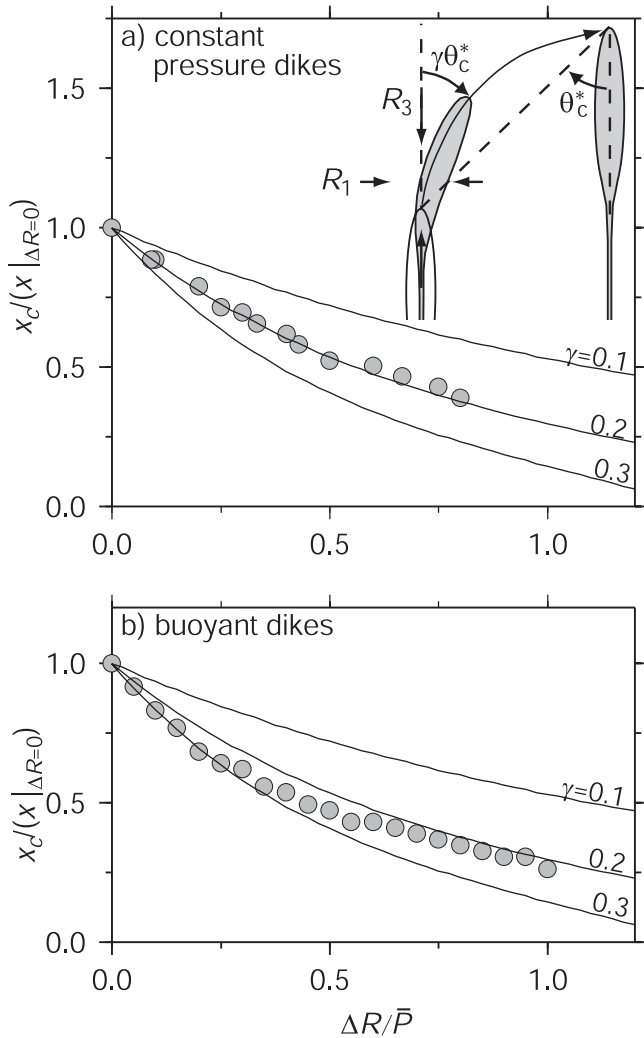


Figure 7. The ratio of the distance of dike connection x_c to that for isotropic remote stresses $x_c|_{\Delta R=0}$ decreases with increasing remote differential stress ΔR normalized by the characteristic driving pressure \bar{P} . Circles show numerical results for (a) constant-pressure dikes and (b) buoyant dikes. The curves are predictions of Griffith's theory (equations (6)–(9)) in which the stress intensity ratio changes with ΔR according to equation (14), with $C_2 = 2.5$ and $\gamma = 0.1, 0.2,$ and 0.3 .

the dike pressure in excess of $-R_1$ (R_1 is negative when compressive) at the start of the calculation. We vary the ratio $\Delta R/\bar{P}$ and measure how x_c decreases compared to its maximum value when $\Delta R = 0$ (i.e., $x_c|_{\Delta R=0}$). The results of both constant-pressure and buoyant dikes are shown Figures 7a and 7b, respectively. In both cases $x_c/(x_c|_{\Delta R=0})$ is roughly halved when $\Delta R/\bar{P} = 0.5$, and both suggest a reduction of $x_c/(x_c|_{\Delta R=0})$ to 0.25 as $\Delta R/\bar{P}$ approaches 1.0. These results demonstrate that a relative decrease in the remote horizontal compressive stress will tend to inhibit the interaction of vertical dikes, as consistent with the results of *Olson and Pollard* [1989] and confirm the reasoning of *Takada* [1994a].

[35] To explain the dependence of $x_c/(x_c|_{\Delta R=0})$ on $\Delta R/\bar{P}$, we again use Griffith's crack theory. Including the effects of

remote differential stresses, we define the average stress intensity ratio as

$$(K_{II}/K_I)^* = C_1 F(L_A/L_B) \frac{\bar{P}_A}{\bar{P}_B} - C_2 \frac{\Delta R}{2\bar{P}_B} \sin(2\gamma\theta_c^*), \quad (14)$$

where C_2 and γ are constants. The second term on the right-hand-side includes the normalized shear driving stress imposed by the remote field on a plane at an angle $\gamma\theta_c^*$ from the least principal remote stress R_3 . A positive angle $\gamma\theta_c^*$, as shown in Figure 7, leads to a decrease in $(K_{II}/K_I)^*$ with increasing ΔR . With $\gamma < 1.0$, $\gamma\theta_c^*$ represents an average orientation of dike B, intermediate between 0 and θ_c^* .

[36] To compare Griffith's crack theory with the numerical results we vary K_{II}/K_I in equations (8) and (9) by varying ΔR in equation (14) for $\bar{P}_A/\bar{P}_B = L_A/L_B = 1.0$, and trial values of C_2 and γ . As done with the numerical results, we plot $\tan(\theta_c)$, normalized by $\tan(\theta_c)|_{\Delta R=0}$ as a function of $\Delta R/\bar{P}$. Figure 7 demonstrates that the net propagation path of dike B can be well explained by predictions from (8)–(9), with the average stress-intensity ratio $(K_{II}/K_I)^*$ defined by (14). The example calculations shown are for $C_2 = 2.5$ and $\gamma = 0.1, 0.2,$ and 0.3 . These values of C_2 and γ are not unique as the results depend on a trade-off between the two quantities; however, bounds of $C_2 = 2-3$ and $\gamma = 0.15-0.25$ generate root-mean square misfits between the theoretical curves and numerical results of $< \sim 0.03$. We note also that C_2 and γ may change for different values of \bar{P}_A/\bar{P}_B and L_A/L_B . This analysis demonstrates that increasing the remote differential stress decreases K_{II} relative to K_I . This moves dike B down the curve predicted by Griffith's crack theory (Figure 5b) and causes the trajectory to curve less.

5. Application to Multiple Dike Systems

[37] One application of our above model of dike interaction is to examine how dike interaction can influence magma transport in a system of many dikes. Using numerical models, we begin with a statistically uniform distribution of multiple dikes, as might arise in a laterally broad source region. The dikes we simulate have tails that are being fed with a constant flux from an arbitrary magma source. We then quantify how the distribution of magma in dikes changes as dikes ascend and interact. The parameter we vary is the initial average spacing between dikes \bar{x}_0 . We examine the case of an isotropic remote stress field to show the maximum effect of dike interaction.

5.1. Method

[38] We use the same numerical method as in our two-dike models but with some modifications. First, we solve for the propagation direction of many dikes (in the examples shown we use twenty). For simplicity, we assume that the dike heads have the same initial length L and the same driving pressure gradient dP/dy . We initiate the dikes parallel to each other and use a random number generator to define initial dike separations between a specified minimum and maximum value. A minimum separation of $0.1L$ ensures numerical stability and the maximum separation is twice the desired mean spacing \bar{x}_0 . Random positions are set

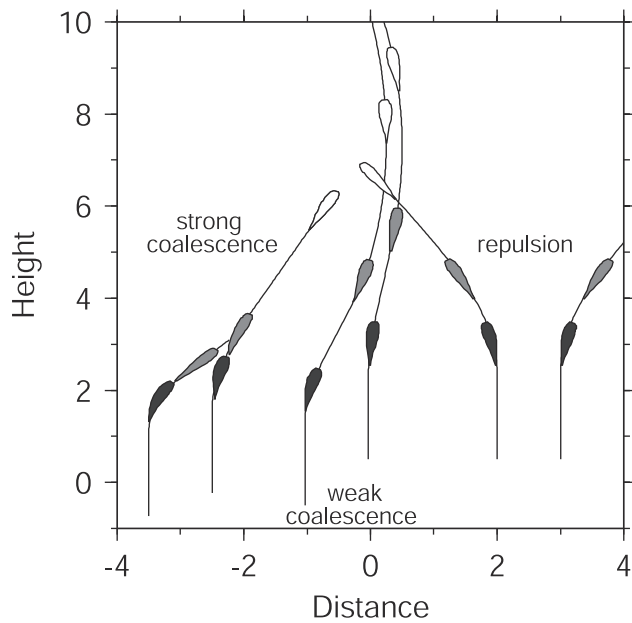


Figure 8. Dike propagation paths of three different calculations, each involving two dikes propagating at the same rate. Horizontal separation is arbitrarily set at $1.0L$, and vertical offset is varied. Shapes (dike thicknesses exaggerated for clarity) and positions of dike heads are shown at start of calculation (darkest) and at two arbitrary time steps (gray and white).

repeatedly until the average spacing of dikes is within 2% of \bar{x}_0 . We assign the vertical positions of the upper dike tips by sampling at random from a uniform distribution of vertical coordinates between zero (referenced to the initial bottom of the deepest dike) and a maximum value, arbitrarily set to $2L$.

[39] The second set of modifications allows dike heads to intersect dike tails. We again do not explicitly specify stress boundary conditions along the tails of dikes but we do track tail locations by recording the propagation path behind the dike heads. When a dike head (dike B) intersects a tail of another dike (dike A), we assume that the magma of dike B is immediately incorporated into dike A. To simulate drainage of dike B into dike A, we remove dike B from the calculation and increase dike A's flux by that of dike B. For simplicity, we ignore any transitory or long-term changes in driving pressure or dike head length due to dike intersections and associated changes in dike flux.

[40] We do include, however, associated changes in propagation rate. This is our final modification. Propagation rate V is controlled by equation (2), and the magma flux Q feeding a dike is the product VW . Dikes fed by a constant flux will thus rise at a rate

$$V = \left(\frac{\Delta\rho g}{12\eta} \right)^{1/3} Q^{2/3}. \quad (15)$$

As flux increases due to intersection with other dikes, so will ascent rate. We model differences in propagation velocity for each dike by scaling the number of time steps between propagation increments inversely with velocity.

[41] We begin each calculation with twenty dikes. As the dikes ascend and interact we record the number of dikes, the height of the center-of-mass of the dike heads (average vertical coordinate of dike heads, weighted by its cross-sectional area), the average flux of the dikes \bar{Q} , and the average horizontal spacing between adjacent dike heads \bar{x} . We end the calculations when the center of mass of the heads rises by a height of $15L$, as few intersections occur beyond this point.

5.2. Results

[42] Allowing dikes to propagate at comparable rates adds interesting complexity to dike interaction. For example, consider two dikes of the same size and propagation rate. Dike B curves, but it also causes dike A to curve. We find three general classes of interaction that, in addition to initial horizontal separation, depend on the initial vertical offset of the two dikes (Figure 8). ‘‘Strong’’ coalescence is characterized by connection of two dikes within a propagation distance of ten dike head lengths. This occurs, for example, when horizontal spacing $x_0 = 1.0L$ and when their initial vertical offset is ~ 0.1 to $1.0L$. ‘‘Weak’’ coalescence refers to connection, but only after the dikes ascend more than ten head lengths. For $x_0 = 1.0L$, this class of interaction occurs if the initial vertical offset exceeds $1.0L$. The last class of interaction actually results in repulsion of the two dikes. Repulsion occurs over all horizontal separations in which dike interaction is important and when the vertical offset is less than $\sim 0.1L$. These different behaviors illustrate the complexity of dike interaction and motivate a statistical characterization of multiple dike systems.

[43] Figures 9a and 9c show starting positions and ensuing dike paths of two example calculations (note that the figures have different horizontal scales). The first model has a starting average dike separation of one dike head length ($\bar{x}_0/L = 1$). Dike interaction causes a great majority of the dikes to coalesce rapidly (Figure 9a). In this example, after the center of mass rises a height $\sim 5L$ (above the starting height of $1.8L$), coalescence increases average dike spacing \bar{x} to $\sim 3.5\bar{x}_0$ and increases average flux \bar{Q} to $\sim 2.5\bar{Q}_0$ (Figure 9b). After rising by a height of $15L$, average separations exceed $\sim 8L$, average flux is $5.5\bar{Q}_0$, and no more dike intersections occur. In addition, as a result of repulsion there is a tendency for dikes to bend outward and away from the center of the dike cluster. This tendency also increases the average separation and is most important when $\bar{x}_0 \leq 2L$.

[44] In the second example $\bar{x}_0 = 5L$. Because \bar{x}_0 is large, few dikes intersect and the dike trajectories remain nearly vertical (Figure 9c). The total increase in the average flux is small (33%) as is the increase in average separation (35%). The contrast between this calculation and the previous demonstrates the sensitivity of dike interaction to initial dike spacing.

[45] We ran different calculations for each \bar{x}_0 20 value for ranging from $0.5L$ to $10L$. For each value of \bar{x}_0 we compute the final average spacing \bar{x}_f and flux \bar{Q}_f . Figure 10a shows how normalized final spacing \bar{x}_f/L changes with normalized initial spacing \bar{x}_0/L . A line with a slope of one would occur if no dike interaction occurs. For $\bar{x}_0 < 3L$, \bar{x}_f exceeds \bar{x}_0 significantly. For $\bar{x}_0 \geq 3L$ the average final spacing still exceeds the initial spacing but the percentage of change in average spacing is small. The above results are even better

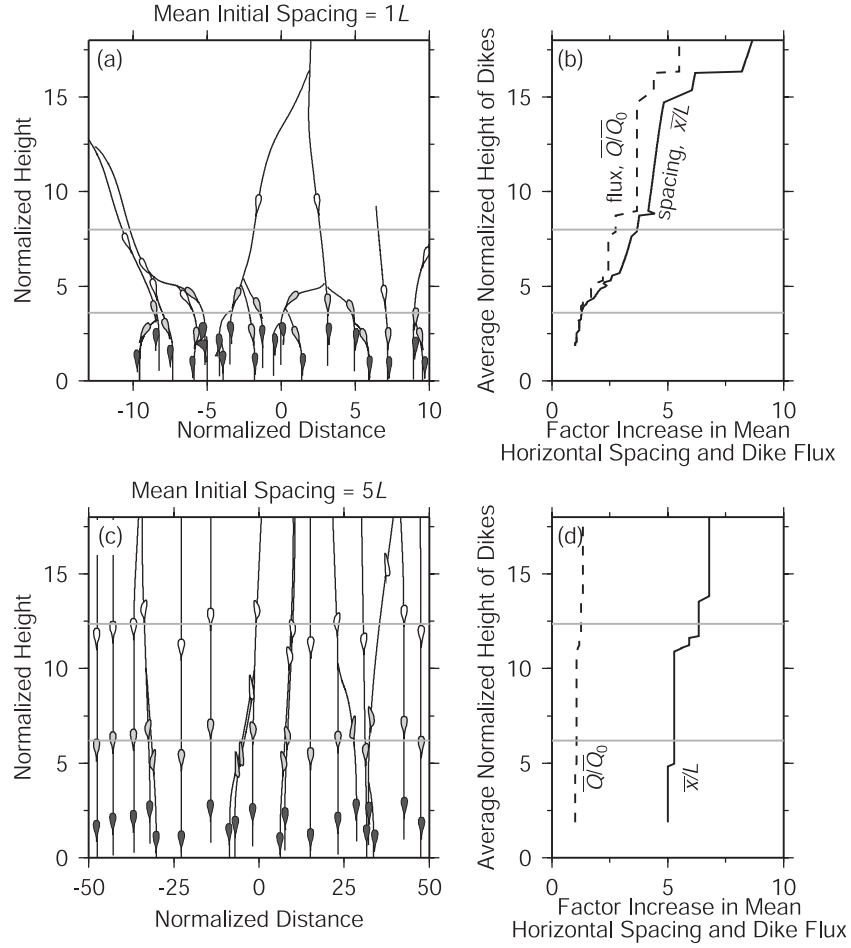


Figure 9. (a) Initial positions (dark), positions at two arbitrary time steps (gray and white) and dike paths of an example numerical calculation involving multiple dikes. Here, the average initial horizontal spacing is one dike head length L . Horizontal and vertical scales are normalized by L . The lower and upper horizontal (gray) lines denote the center of mass corresponding to the gray and white symbols, respectively. (b) Factor increase in average dike flux (dashed) and horizontal spacing (solid) as a function of the normalized height of the dikes' center of mass. (c) and (d) The same as Figures 9a and 9b, respectively, but for a case in which the initial average spacing is $5L$. Note the change in horizontal scale for Figure 9c.

reflected in a plot of \bar{x}_f/\bar{x}_0 (Figure 10b). For $0.5 \leq \bar{x}_0 < 3L$, dike interaction strongly changes the distribution of magma, leading to $\bar{x}_f/\bar{x}_0 = 3-27$. For $\bar{x}_0 \geq 3L$, however, few dikes intersect and \bar{x}_f/\bar{x}_0 remains near one. The best fitting asymptotic function for the distribution in Figure 10b is

$$\bar{x}_f/\bar{x}_0 = 8.32(\bar{x}_0/L)^{-1.98} + 1.0. \quad (16)$$

[46] The changes in average dike flux show a corresponding behavior. Average final fluxes are 2–4 times greater than the starting fluxes for $0.5 \leq \bar{x}_0 < 3L$ (Figure 10c). For $\bar{x}_0 \geq 3L$ dikes interact weakly and final fluxes change very little. The final average fluxes are well fit by the function

$$\bar{Q}_f/\bar{Q}_0 = 2.95(\bar{x}_0/L)^{-1.43} + 1.0. \quad (17)$$

[47] Like the results for interaction of two dikes, the above results for multiple dike interaction predict a separation distance beyond which focusing of magma is unimportant. For multiple 2-D dikes, this spacing \bar{x}_0 is ~ 3 dike lengths (Figures 10b and 10c). This length scale is roughly a factor of 2–3 larger than the maximum distance of intersection of $x_c = 1.2L$ for two (2-D) dikes of equal buoyancy and volume (the rightmost circle in Figure 6b). The factor of 2–3 reflects enhanced interaction when all dikes propagate at comparable rates. We also note that over the range of \bar{x}_0/L examined, there appears to be a minimum final average spacing of $\sim 6L$ at $\bar{x}_0 \sim 3L$ (Figure 10a). This finding suggests that a system of dikes will organize to a spacing of at least $\sim 6L$.

[48] The critical average spacing for significant interaction of multiple, 3-D dikes can be inferred from the difference in x_c found between laboratory (3-D) and numerical (2-D) results of two interacting dikes. A factor of 0.64 (see

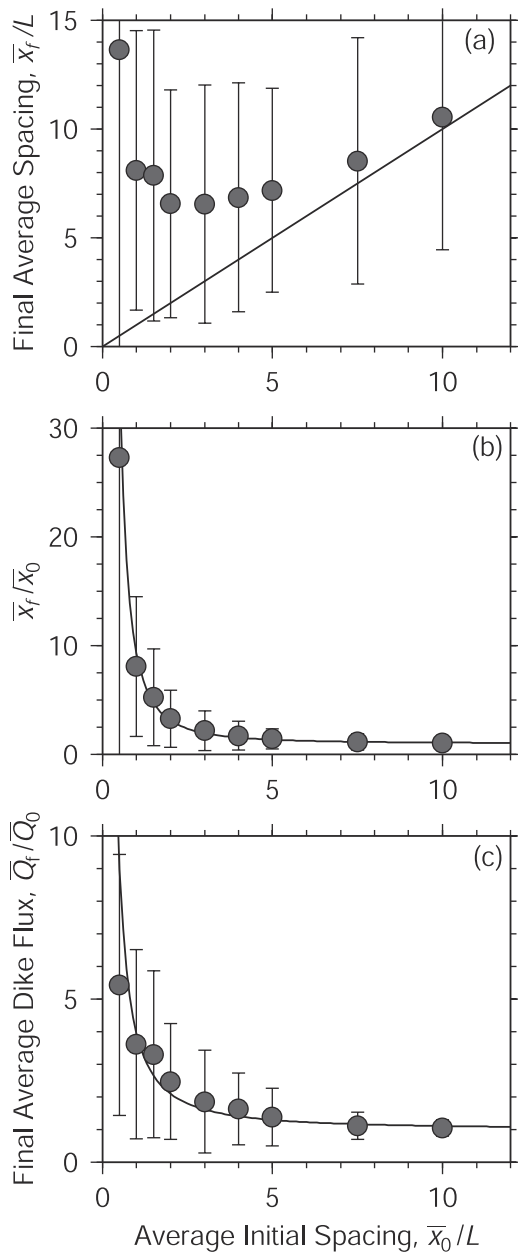


Figure 10. Results of multiple-dike calculations are plotted for different values of normalized, initial average horizontal spacing \bar{x}_0/L . Each symbol is an average of twenty different calculations each involving twenty dikes. Error bars indicate standard deviations. (a) Average horizontal spacing of at the end of calculations \bar{x}_f/L . The solid line with a slope of one is predicted if no dike interaction occurs. (b) Final average spacing \bar{x}_f normalized by \bar{x}_0 is shown with best fitting curve (Equation (16)). (c) Final average volume is normalized by the initial volume (Q_f/Q_0) and shown is best fitting curve (equation (17)).

section 3.2) suggests a critical value of \bar{x}_0 of $x_c \sim 2L$ for 3-D dikes. Likewise, the minimum final spacing \bar{x}_f for 3-D dikes is predicted to be $\sim 4L$. Finally, we note that the case examined here applies to the case in which the remote differential stress is small compared to dike driving pressure. Critical separation and magma focusing distances will

likely decrease with increasing differential remote stress in a fashion similar to predictions shown in Figure 7b.

6. Application to Natural Magmatic Systems

6.1. Length and Pressure Scales Required for Strong Dike Interaction

[49] As demonstrated above, dike head length L is the key length scale controlling the distances over which dike interaction can focus magma. A minimum dike head length of $L = L_c$ occurs when the dike head contains just enough magma such that $K_I = K_c$. From equation (7) and for $\bar{P} = \Delta\rho gL/2$, this critical length is

$$L_c = 2 \left(\frac{K_c}{C\Delta\rho g} \right)^{2/3}. \quad (18)$$

Experimental determinations of K_c for basalt, gabbro, and dunite are in the range of 0.84–3.75 MPa m^{1/2} [Atkinson and Meredith, 1987]. A value of $K_c = 3$ MPa m^{1/2} and $g = 0.0039$ MPa/m (i.e., magma density of 2900 kg/m³ and mantle density of 3300 kg/m³) implies $L_c \sim 10^2$ m for 2-D dikes and $\sim 50\%$ greater for penny-shaped dikes. For small dike fluxes, dike head lengths are predicted remain close to this length [Rubin, 1998]. This condition is met when the thickness of the tail is less than the thickness scale

$$W_c = \frac{3\sqrt{3}}{4C^{4/3}} \frac{(1-\nu)}{\mu} \frac{K_c^{4/3}}{(\Delta\rho g)^{1/3}}. \quad (19)$$

This thickness scale is the maximum thickness of a dike head [Secor and Pollard, 1975] with $L = L_c$ as given by (18). For 2-D dikes, the above values for K_c , $\Delta\rho g$, and for an elastic stiffness $\mu/(1-\nu)$ of 5×10^4 MPa yield $W_c = 3 \times 10^{-4}$ m. For thicker dikes associated with larger magma fluxes, dike head length can be several times L_c [Rubin, 1998]. Thus, for 2-D dikes we predict dike interaction to be capable of focusing magma over distances x_c of at least $6L_c \sim 6 \times 10^2$ m if initial spacing is within $\sim 3 \times 10^2$ m and the remote differential stress field is negligible compared to \bar{P} . These lengths are expected to be comparable for 3-D dikes.

6.2. Implications for Magma Transport in the Asthenosphere Beneath Mid-ocean Ridges

[50] The above models predict magma focusing by dike interaction to be important when two conditions are met: (1) the differential stress of the remote field is small compared to the characteristic driving pressure of dike heads and (2) dike heads are spaced, horizontally as well as vertically, less than a few dike head lengths apart. We here examine under what conditions that the two above criteria will be met. As an example, we consider the partially molten zone beneath mid-ocean ridges.

6.2.1. Remote Differential Stresses in the Mantle

[51] The first criterion is an important limitation on dike coalescence. For small dikes of head length comparable to L_c , the pressure gradient in the head is approximately hydrostatic. A dike with a minimum head length of 10^2 m would have a characteristic driving pressures of $\bar{P} = \Delta\rho gL/2 = 0.2$ MPa. The lithospheric mantle is capable of supporting much greater differential stresses. For example, lithospheric

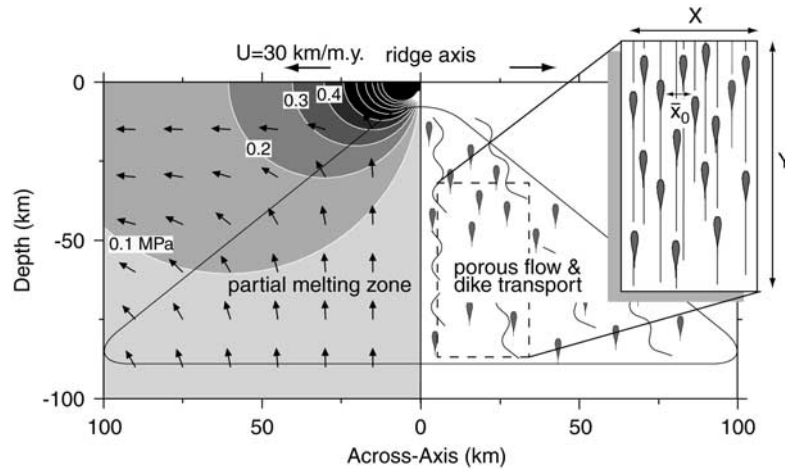


Figure 11. (left) Mantle flow (arrows) and differential stress (contoured at 0.1 MPa intervals) caused by two diverging top boundaries, which represent spreading plates at a mid-ocean ridge. The half spreading rate is U . (right) Schematic illustration of melt migrating upward from the melting zone. Magma is transported in dike heads (gray symbols) and in intergranular pores. Box in the upper right illustrates the conceptual model in which dikes are distributed in an arbitrary area of dimensions X and Y . Dike tails are shown as solid lines.

stresses due to volcanic loads [Muller *et al.*, 2001] and the associated plate flexure [ten Brink, 1991] can be tens of megapascals. Thus dike interaction in the lithosphere can strongly focus magma only beneath very small volcanic loads or in regions where the differential remote stress is $< \sim 0.2$ MPa.

[52] Remote differential stresses can be much lower in low-viscosity asthenosphere. Beneath mid-ocean ridges, asthenospheric corner flow driven by plate spreading generates differential stresses given in cylindrical coordinates (r, θ) with origin at the ridge axis [Sleep, 1984],

$$\Delta R = (4\eta_a U / \pi r) \sin(\theta). \quad (20)$$

Figure 11 illustrates the differential stress field due to a ridge spreading with an intermediate half rate of $U = 0.03$ m/yr and asthenosphere viscosity $\eta_a = 10^{19}$ Pa s [e.g., Hirth and Kohlstedt, 1996]. In this reference calculation, $\Delta R < 0.2$ MPa throughout most of the area encompassing a hypothetical melting zone [e.g., Reid and Jackson, 1981; Phipps Morgan, 1987; Scott and Stevenson, 1989; Sotin and Parmentier, 1989]. Only very close to the ridge axis does ΔR exceed 0.2 MPa. As ΔR is proportional to U and η_a , faster spreading rates and greater asthenospheric viscosities would constrict the area over which dike interaction can be important. Likewise, lower spreading rates and asthenospheric viscosities would allow for a broader area of dike interaction at the same spreading rates. Although the mantle flow field and viscosity beneath mid-ocean ridges is poorly known, this calculation shows an example scenario in which ΔR is sufficiently small to allow for dike interaction over an appreciable area of the melting zone.

6.2.2. Conditions for Small Spacing of Dikes Beneath Mid-ocean Ridges

[53] We now examine the conditions that would allow for dike spacing small enough to allow for strong dike coa-

lescence. This leads to the question of how dikes form and grow out of partially molten systems. Such processes involve the coupling of melt migration, matrix deformation, elasticity, and fracturing, of which few studies have addressed together. Rubin [1998] suggests that, in the absence of any freezing boundaries, dikes can initiate by a combination of subcritical propagation and interconnection of melt-filled tubules along grain boundaries. Such a process requires sufficient localization of magma. Plausible mechanisms for the localization of melt include melt channeling associated with matrix shear [Stevenson, 1989; Richardson, 1998; Zimmerman *et al.*, 1999] and feedback between matrix permeability and dissolution [Aharanov *et al.*, 1995; Kelemen *et al.*, 1995a, 1995b]. If dikes arise out of porosity channels then we would expect initial horizontal spacing between dikes to be similar to the wavelengths of channel instabilities. Wavelengths of reaction infiltration instabilities are expected to be 1–200 m [Aharanov *et al.*, 1995; Spiegelman *et al.*, 2001], whereas channels formed by shear deformation in a matrix with melt-dependent viscosity are expected to be separated by meters [Stevenson, 1989]. If dikes arise from either mechanisms of melt localization then the initial horizontal spacing is likely to be small enough for dike interaction to strongly focus melt.

[54] We require, however, that both horizontal and vertical separation be small for dike interaction to be important. We examine the conditions for this possibility with the following elementary calculations. A large simplification that we make is that dike properties such as thickness, ascent rate, tail length, spacing, etc. can be represented by characteristic or average values, even though such properties may change significantly with depth depending on the physics involved. Our objective in making this simplification is to generalize our application such that it embodies a range of conditions of dike growth and ascent in partially molten mantle. In particular, we will determine the characteristic thicknesses W and ascent rates V that will allow for

average horizontal and vertical spacing between dike heads to be $\sim 10^2$ m.

[55] We imagine a scenario in which dike heads are forming throughout an arbitrary area in the mantle undergoing partial melting of horizontal and vertical dimension X and Y , respectively. We assume the total number of dikes n in the region remains at a constant steady state value. The average vertical cross-sectional area surrounding each dike is XY/n and the average spacing between the dikes is

$$\bar{x}_0 = (XY/n)^{1/2}. \quad (21)$$

[56] At the top of the melting domain being considered, n_x dikes with characteristic flux Q would be required to remove a fraction f of the total melt generated in the region and thus

$$n_x Q = f \dot{M} XY \quad (22)$$

where \dot{M} is melting rate. Here Q is controlled by laminar flow of magma ascending at a characteristic rate V through the top of the average thickness W . From equation (2),

$$Q = VW = (\Delta\rho g / 12\eta) W^3 = (12\eta / \Delta\rho g)^{1/2} V^{3/2}. \quad (23)$$

[57] Note that n_x increases with vertical dimension Y in equation (22) in order to extract a magma flux proportional to the area XY undergoing melting. For this same reason the number of dikes spanning X at any vertical position also increase linearly from zero at the base of the melting area to n_x at the top of the melting area. The height Y divided by the average vertical separation between dike heads yields the number of dikes n_y that would span the vertical dimension Y of the melting area. The total number of dikes in the melting area is therefore

$$n = 1/2(n_x n_y). \quad (24)$$

The factor of 1/2 accounts for the linear increase in the number of dikes spanning the width X with increasing height in the melting area.

[58] To quantify n_y , we assume that dike heads traverse a vertical distance Vt_T , in the time t_T it takes the lower tip of the tail to terminate. We consider a portion of the tail “terminated” when it is so narrow that its presence no longer perturbs the ambient permeability of the surrounding matrix (see Appendix A for derivation of t_T). If n is to remain constant, the rate that dikes are terminating must equal the rate that new dike heads are forming. The termination timescale t_T is therefore also the timescale for new dike heads to form and

$$n_y = Y/Vt_T. \quad (25)$$

Substituting equations (22)–(25) into equation (21) yields the average spacing

$$\bar{x}_0 = \left[\frac{2(\Delta\rho g / 12\eta)^2 W^5 t_T}{f \dot{M} Y} \right]^{1/2} = \left[\frac{2(12\eta / \Delta\rho g)^{1/2} V^{5/2} t_T}{f \dot{M} Y} \right]^{1/2} \quad (26)$$

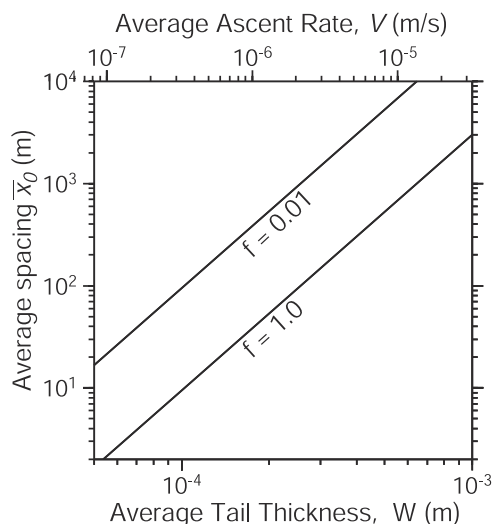


Figure 12. Average spacing of dike heads transporting a fraction f of the total melt in an arbitrary region in the mantle undergoing partial melting as a function of tail thickness W .

As the above description omits the effects of dike interaction (which could clearly change the average spacing) equation (26) describes average spacing in the absence of, or prior to, dike interaction.

[59] Using equation (26), we can estimate the range of average dike tail thicknesses and ascent rates that will allow for average spacing to be $\sim 10^2$ m. We take $Y = 7.5 \times 10^4$ m to be the depth of the partial melting zone and assume $t_T = 10^9$ s (see Appendix A). For melting rate, we assume mantle is upwelling at $U = 0.03$ m/yr and melting to a maximum degree of 25% over the depth interval Y (yielding a melt productivity of $\sim 1\%$ /kbar of decompression [Langmuir *et al.*, 1992]) such that $\dot{M} = U(0.25/Y) = 3.17 \times 10^{-15} \text{ s}^{-1}$. Figure 12 shows average separations \bar{x}_0 over a range of values of W and V for $f = 0.01$ and 1.0. These calculations demonstrate that strong dike interaction requires small dikes, with tail thicknesses comparable to or less than W_c .

[60] Are such minimal sizes likely to represent an average dike size in the partially molten mantle? Indeed, prior to growth by dike interaction, minimal fluxes are to be expected for new dikes forming out of intergranular tubules. On the other hand, dikes may grow independent of dike interaction by porous melt flow from the surrounding matrix in through the dike walls. Rubin [1998] predicts that such a process can increase the dike thickness to many times W_c . Rubin’s [1998] calculations, however, considered isolated dikes drawing magma from an infinitely large region of partially molten magma. In contrast, a population of many dikes will be forced to compete for magma in the intervening matrix and therefore grow at a lower rate than predicted by Rubin [1998].

[61] Geochemical and geophysical observations may provide ways to test and constrain some aspects of the above predictions. For example, a characteristic ascent rate of $\sim 10^{-6}$ m/s (~ 3 m/yr), which allow for $\bar{x}_0 \sim 10^2$ (Figure 12), is consistent with the estimated magma ascent

rates needed to explain the observed Th and Ra activity excesses in erupted basalts [e.g., *Spiegelman and Elliott, 1993; Kelemen et al., 1997*]. The volume fraction of melt in the mantle (i.e., porosity) is another useful constraint. Dikes of thicknesses equal to W_c and separated by 10^2 m would represent only a small fraction ($<10^{-5}$) of mantle volume. Low seismic speeds imaged in the MELT region of the East Pacific Rise, however, suggest volume fractions of $1-5 \times 10^{-2}$ [*Toomey et al., 1998; Webb and Forsyth, 1998*]. It is thus possible that intergranular flow may account for most of volume fraction of melt sitting in mantle, whereas dikes transport may contribute significantly to the flux of magma flowing through the mantle. This is a possible explanation for the discrepancy between the low volume fraction estimates of geochemical studies (e.g., $\sim 10^{-3}$ [*Johnson and Dick, 1992*]), compared to those estimated from seismic observations. Melt composition is sensitive to the relative flux of melts arriving at the ridge axis, whereas seismic observations are sensitive to the volume of melt in the mantle.

6.3. Interaction of Crustal Dikes at Mid-ocean Ridges?

[62] Section 6.2 describes the requirements for dike interaction in the partial melting region of the mantle beneath mid-ocean ridges. We now discuss the potential importance of dike interaction in the crust. Interacting dikes in the crust need not be molten at the same time. Because a frozen dike can still maintain the driving pressure at which it was emplaced, old diking events could attract magma and localize eruptions of subsequent diking events. The possibility of such interaction depends on the magnitude of the remote differential stress field ΔR compared to the characteristic driving pressures of dikes. In extensional settings such as mid-ocean ridges, ΔR is large. However, dike driving pressures are also large (i.e., tens of megapascals) as suggested by dike thicknesses of meters [*Nicolas, 1986; Francheteau et al., 1990; Hurst et al., 1994; Gudmundsson, 1995*] and inferred heights of $L \sim 1$ km. The ambient differential stress ΔR is likely to depend on many factors including the rheological structure of the crust [*Chen and Morgan, 1990; Shaw and Lin, 1996; Poliakov and Buck, 1998*], the frequency and geometry of faults [*Forsyth, 1992; Shaw and Lin, 1996*], as well as the frequency of diking events [*Perfit and Chadwick, 1998*]. The likelihood that tectonic versus magmatic extension may be episodic [*Malinverno and Pockalny, 1990; Thatcher and Hill, 1995; Macdonald et al., 1996*] suggests $\Delta R/\bar{P}$ in the crust at mid-ocean ridges is also likely to be a complex function of time.

[63] One hint that dike interaction may be important in the crust is the observation that fast spreading ridges typically have narrower neo-volcanic zones than slow spreading ridges [e.g., *Perfit and Chadwick, 1998*]. A number of observations are consistent with a smaller $\Delta R/\bar{P}$ at fast- compared to slow spreading ridges. For example, fast spreading ridges typically have narrower axial summit grabens [*Chadwick and Embley, 1998*], smaller faults [*Small, 1998*], a larger contribution of topography associated with constructional volcanism [*Lonsdale, 1977; Macdonald and Atwater, 1978; Lewis, 1979; Macdonald, 1982; Shaw and Lin, 1993; Macdonald et al., 1996; Small, 1998*], and a greater degree of magmatic,

relative to tectonic extension [*Macdonald et al., 1992; Perfit and Chadwick, 1998*]. Lower values of $\Delta R/\bar{P}$ at fast spreading ridges would promote greater magma focusing by dike interaction and could confine eruptions closer to the ridge axis.

7. Conclusions

[64] Laboratory experiments and numerical calculations show that two adjacent buoyant dikes will tend to merge as they interact if they are spaced closely enough. The maximum distance that one dike (B) will intersect another (A) is well explained by predictions of Griffith energy theory. When the remote differential stress is small compared to dike driving pressure, the maximum distance of intersection for two dikes of equal length and driving pressure is ~ 1.2 dike head lengths for 2-D dikes and ~ 0.8 dike head lengths for 3-D dikes. The maximum distance of intersection decreases with increasing remote differential stress. Interaction among multiple dikes is strongest when the initial average spacing is within ~ 3 dike head lengths. When interaction is strong, dike coalescence leads to horizontal spacing of at least ~ 6 head lengths and can dramatically increase average dike flux. Focusing of magma by dike interaction is possible beneath mid-ocean ridges if the asthenospheric viscosity is low ($\leq \sim 10^{19}$ Pa s) and if dike heads are present in the partial melting zone with average spacing 10^2 m or less. Whether dike interaction focuses magma in the crust remains speculative and depends on the relative magnitudes of tectonic stresses and dike driving pressures.

Appendix A: Timescale for Dike Tail Termination

[65] Magma flow through a dike tail is described as viscous flow through a thin slot. A dike no longer being fed by magma source or by porous flow, will thin as the dike head rises. As the tail thickness approaches zero, so does the magma ascent rate; therefore magma will always be present in tail. At some thickness, however, the flux of magma through the tail may become indistinguishable from the flux of magma through the ambient porous mantle matrix. At this thickness we consider the tail to terminate. We first derive the termination thickness, and then the time it takes the tail to reach this thickness.

[66] The percolation flux of magma per cross-sectional area of mantle V_D (i.e., Darcy flow rate) through a matrix with permeability k is described by

$$V_D = k \Delta \rho g / \eta. \quad (\text{A1})$$

Matrix permeability is determined by the geometry and shape of interconnected pore space. For interconnecting tubes at grain junctions,

$$k = \frac{\phi^2 b^2}{72\pi} \quad (\text{A2})$$

[*Turcotte and Schubert, 1982*], where ϕ is porosity and b is grain size. Dike termination occurs when the tail does not change the permeability of the surrounding porous matrix. Following arguments similar to those of *Turcotte and*

Schubert [1982], parallel 2-D dike tails separated by a distance b would have a permeability

$$k = \frac{W^3}{12b}, \quad (\text{A3})$$

where W is dike tail thickness. Equating equations (A2) and (A3) defines the termination thickness

$$W_T \equiv b \left(\frac{\phi^2}{6\pi} \right)^{1/3}. \quad (\text{A4})$$

For matrix porosities of 0.01–0.05 and $b = 10^{-3}$ m, the respective termination thicknesses are $2\text{--}5 \times 10^{-5}$ m.

[67] The time it takes the tail walls to reach the termination thickness depends on the rate at which there is a net loss of magma in that portion of the tail. This depends on the process by which melt accumulates to form and grow a dike. Rubin [1998] proposes that dikes are fed by porous influx of magma from the matrix through the dike walls. As magma is squeezed from the mantle into the dike, pore pressure diffuses from high values far from the dike to a constant, minimum value at the dike wall. This process can be described by a 1-D diffusion equation of pore pressure (equation (B9) of Rubin [1998]). The pore pressure diffusivity D can be used to estimate a time t it takes adjacent dikes to drain the intervening matrix of magma, after which there is minimal flux into a dike,

$$t = \bar{x}_0^2/D \quad (\text{A5})$$

The parameter values of Rubin [1998] predict a diffusivity of $D = 4 \times 10^3$ m²/s. For an average spacing of $\bar{x}_0 = 10^2$ m (which will allow for strong dike interaction), the intervening matrix will be drained in $\sim 10^6$ s, after which the dike will begin to lose magma and thin. The above is an absolute minimum estimate of termination time because more time is required for the dike to thin to the termination thickness.

[68] To estimate the time it takes to reach the termination thickness after the matrix between dikes has been drained, we consider the evolution of a dike of constant volume. An initially 2-D ellipsoidal pocket of magma will lengthen vertically due to magma buoyancy. As it does so, it will thin in order to conserve volume [Spence and Turcotte, 1990]. Using equation (13) of Spence and Turcotte [1990] the time required for a point along the dike to thin from an initial thickness W to W_T is

$$t'_T = (1 + y')(W_T'^{-2} - W'^{-2}). \quad (\text{A6})$$

Here, the primes denote dimensionless quantities in which we normalize height y by L_c (equation (18)), thicknesses by W_c (equation (19)), and time by the timescale $L_c(\eta/\Delta\rho g W_c^2) = 3 \times 10^6$ s. For $y' = W' = 1$ and termination thicknesses W_T' of 5×10^{-5} m and 2×10^{-5} m, the respective termination times are $t_T = 2 \times 10^8$ s (6 years) and $t_T = 2 \times 10^9$ s (60 years).

[69] **Acknowledgments.** The laboratory experiments benefited from discussions with and laboratory facilities provided by D. Bercovici, T. Menand, and A. Takada provided helpful reviews, and Associate Editor A. Rubin contributed particularly poignant comments that greatly strengthened this manuscript. This study was supported by the SOEST Young Investigator Program, a University of Hawaii, URC seed grant, and NSF-OCE97-30673.

References

- Aharanov, E., J. Whitehead, P. B. Kelemen, and M. Spiegelman, Channeling instability of upwelling melt in the mantle, *J. Geophys. Res.*, **100**, 20,433–20,450, 1995.
- Anderson, E. M., The dynamics of the formation of cone-sheets, ring-dykes and cauldron-subsidences, *Proc. R. Soc. Edinburgh*, **56**, 128–157, 1936.
- Atkinson, B. K., and P. G. Meredith, Experimental fracture mechanics data for rocks and minerals, in *Fracture Mechanics of Rock*, edited by B. K. Atkinson, pp. 477–525, Academic, San Diego, Calif., 1987.
- Cannat, M., How thick is the magmatic crust at slow spreading oceanic ridges?, *J. Geophys. Res.*, **101**, 2847–2857, 1996.
- Chadwick, W. W., Jr., and R. W. Embley, Graben formation associated with recent dike intrusions and volcanic eruptions on mid-ocean ridges, *J. Geophys. Res.*, **103**, 9807–9825, 1998.
- Chen, R., and W. J. Morgan, A nonlinear rheology model for mid-ocean ridge axis topography, *J. Geophys. Res.*, **95**, 17,583–17,604, 1990.
- Crouch, S. L., and A. M. Starfield, *Boundary Element Methods in Solid Mechanics*, Allen and Unwin, Concord, Mass., 1983.
- Dick, H. J. B., and J. H. Natland, Late stage melt evolution and transport in the shallow mantle beneath the East Pacific Rise, *Proc. Ocean Drill. Program Sci. Results*, **137**, 103–134, 1996.
- Emerman, S. H., and R. Marrett, Why dikes?, *Geology*, **18**, 231–233, 1990.
- Fiske, R. S., and E. D. Jackson, Orientation and growth of Hawaiian volcanic rifts: The effect of regional structure and gravitational stresses, *Proc. R. Soc. London, Ser. A*, **329**, 299–326, 1972.
- Forsyth, D. W., Seismological constraints on partial melting beneath the East Pacific Rise, *Eos Trans. AGU*, **73**(14), Spring Meet. Suppl., 290, 1992.
- Francheteau, J., R. Armijo, J. L. Cheminee, R. Hekinian, P. Lonsdale, and N. Blum, 1 Ma East Pacific Rise oceanic crust and uppermost mantle exposed by rifting in Hess Deep (equatorial Pacific Ocean), *Earth Planet. Sci. Lett.*, **101**, 281–295, 1990.
- Griffith, A. A., The phenomena of rupture and flow in solids, *Philos. Trans. R. Soc. London, Ser. A*, **221**, 163, 1920.
- Griffith, A. A., The theory of rupture, in *Proceedings of the First International Congress on Applied Mechanics*, edited by C. B. Biezeno and J. M. Burgers, p. 55, J. Waltman Jr., Delft, Netherlands, 1924.
- Gudmundsson, A., Infrastructure and mechanics of volcanic systems in Iceland, *J. Volcanol. Geotherm. Res.*, **64**, 1–22, 1995.
- Heimpel, M., and P. Olson, Buoyancy-driven fracture and magma transport through the lithosphere: Models and experiments, in *Magmatic Systems*, edited by M. P. Ryan, pp. 223–240, Academic, San Diego, Calif., 1994.
- Hieronymus, C. F., and D. Bercovici, A theoretical model of hotspot volcanism: Control on volcanic spacing and patterns via magma dynamics and lithospheric stresses, *J. Geophys. Res.*, **106**, 683–702, 2001.
- Hirth, G., and D. L. Kohlstedt, Water in the oceanic upper mantle: Implications for rheology, melt extraction, and the evolution of the lithosphere, *Earth Planet. Sci. Lett.*, **144**, 93–108, 1996.
- Hurst, S. D., J. A. Karson, and K. L. Verosub, Paleomagnetism of tilted dikes in fast spread oceanic crust exposed in the Hess Deep Rift: Implications for spreading and rift propagation, *Tectonics*, **13**, 789–802, 1994.
- Johnson, K. T. M., and H. J. B. Dick, Open system melting and temporal and spatial variation of peridotite and basalt at the Atlantis II fracture zone, *J. Geophys. Res.*, **97**, 9219–9241, 1992.
- Johnson, K. T. M., H. J. B. Dick, and N. Shimizu, Melting in the oceanic upper mantle: An ion microprobe study of diopsides in abyssal peridotites, *J. Geophys. Res.*, **95**, 2661–2678, 1990.
- Kelemen, P. B., N. Shimizu, and V. J. M. Salters, Extraction of mid-ocean-ridge basalt from the upwelling mantle by focused flow of melt in dunite channels, *Nature*, **375**, 747–753, 1995a.
- Kelemen, P. B., J. A. Whitehead, E. Aharanov, and K. Jordahl, Experiments on flow focusing in soluble porous media, with applications to melt extraction from the mantle, *J. Geophys. Res.*, **100**, 475–496, 1995b.
- Kelemen, P. B., G. Hirth, N. Shimizu, M. Spiegeleman, and H. J. B. Dick, A review of melt migration processes in the adiabatically upwelling mantle beneath oceanic spreading centers, *Philos. Trans. R. Soc. London, Ser. A*, **355**, 283–318, 1997.
- Langmuir, C. H., E. M. Klein, and T. Plank, Petrological systematics of mid-ocean ridge basalts: Constraints on melt generation beneath ocean ridges, in *Mantle Flow and Melt Generation at Mid-ocean Ridges*, *Geophys. Monogr. Ser.*, vol. 71, edited by J. P. Morgan, D. K. Blackman, and J. M. Sinton, pp. 183–280, AGU, Washington, D. C., 1992.
- Lawn, B., *Fracture of Brittle Solids*, Second Edition, 378 pp., Cambridge Univ. Press, New York, 1993.
- Lewis, B. T. R., Periodicities in volcanism and longitudinal magma flow on the East Pacific Rise at 23°N, *Geophys. Res. Lett.*, **6**, 753–756, 1979.
- Lister, J. R., Buoyancy-driven fluid fracture: the effects of material toughness and of low-viscosity precursors, *J. Fluid Mech.*, **210**, 263–280, 1990.
- Lister, J. R., The solidification of buoyancy-driven flow in a flexible-walled channel, part 2, Continual release, *J. Fluid Mech.*, **272**, 45–65, 1994.

- Lister, J. R., and R. C. Kerr, Fluid-mechanical models of crack propagation and their application to magma transport in dikes, *J. Geophys. Res.*, *96*, 10,049–10,077, 1991.
- Lonsdale, P., Abyssal pahoehoe with lava coils at the Galapagos rift, *Geology*, *5*, 147–152, 1977.
- Macdonald, K. C., Mid-ocean ridges: Fine scale tectonic volcanic and hydrothermal processes within the plate boundary zone, *Annu. Rev. Earth Planet. Sci.*, *10*, 155–190, 1982.
- Macdonald, K. C., and T. Atwater, Evolution of rifted ocean ridges, *Earth Planet. Sci. Lett.*, *39*, 319–327, 1978.
- Macdonald, K. C., D. S. Scheirer, S. Carbotte, and P. J. Fox, Recent advances in the understanding of mid-ocean ridge tectonics and volcanism using swath-mapping tools, *Acta Geol. Hispanica*, *27*, 13–32, 1992.
- Macdonald, K. C., P. J. Fox, R. T. Alexander, R. Pockalny, and P. Gente, Volcanic growth faults and the origin of Pacific abyssal hills, *Nature*, *380*, 125–129, 1996.
- Malinverno, A., and R. A. Pockalny, Abyssal hill topography as an indicator of episodicity in crustal accretion and deformation, *Earth Planet. Sci. Lett.*, *99*, 154–169, 1990.
- McKenzie, D., The extraction of magma from the crust and mantle, *Earth Planet. Sci. Lett.*, *72*, 1985, 1985.
- Muller, J. J., and S. J. Martel, Numerical models of translational landslide rupture surface growth, *Pure Appl. Geophys.*, *157*, 1009–1038, 2000.
- Muller, J. R., G. Ito, and S. J. Martel, Effects of volcano loading on dike propagation in an elastic half-space, *J. Geophys. Res.*, *106*, 11,101–11,114, 2001.
- Nicolas, A., Melt extraction model based on structural studies in mantle peridotites, *J. Petrol.*, *27*, 999–1022, 1986.
- Nicolas, A., Melt extraction from mantle peridotites: Hydrofracturing and porous flow, with consequences for oceanic ridge activity, in *Magma Transport and Storage*, edited by M. P. Ryan, pp. 159–174, John Wiley, New York, 1990.
- Nicolas, A., F. Boudier, and B. Ildefonse, Dike patterns in diapirs beneath oceanic ridges: The Oman Ophiolite, in *Magmatic Systems*, edited by M. P. Ryan, pp. 77–95, Academic, San Diego, Calif., 1994.
- Olson, J., and D. D. Pollard, Inferring paleostresses from natural fracture patterns: A new method, *Geology*, *17*, 345–348, 1989.
- Olson, J. E., and D. D. Pollard, The initiation and growth of echelon veins, *J. Struct. Geol.*, *13*, 595–608, 1991.
- Perfit, M. R., and W. W. J. Chadwick, Magmatism at mid-ocean ridges: Constraints from volcanological and geochemical investigations, in *Faulting and Magmatism at Mid-ocean Ridges*, *Geophys. Monogr. Ser.*, vol. 106, edited by R. Buck et al., pp. 59–115, AGU, Washington, D. C., 1998.
- Phipps Morgan, J., Melt migration beneath mid-ocean spreading centers, *Geophys. Res. Lett.*, *14*, 1238–1241, 1987.
- Poliakov, A. N. B., and W. R. Buck, Mechanics of stretching elastic-plastic-viscous layers: Applications to slow-spreading mid-ocean ridges, in *Faulting and Magmatism at Mid-ocean Ridges*, *Geophys. Monogr. Ser.*, vol. 106, edited by W. R. Buck et al., pp. 305–323, AGU, Washington, D. C., 1998.
- Pollard, D. D., and P. Segall, Theoretical displacements and stresses near fractures in rock: With applications to faults, joints, veins, dikes, and solution surfaces, in *Fracture Mechanics of Rock*, edited by B. K. Atkinson, pp. 277–349, Academic, San Diego, Calif., 1987.
- Reid, I., and H. R. Jackson, Oceanic spreading rate and crustal thickness, *Mar. Geophys. Res.*, *5*, 165–172, 1981.
- Richardson, C. N., Melt flow in a variable viscosity matrix, *Geophys. Res. Lett.*, *25*, 1099–1102, 1998.
- Roering, J. J., M. L. Cooke, and D. D. Pollard, Why blind thrust faults do not propagate to the Earth's surface: Numerical modeling of coseismic deformation associated with thrust-related anticlines, *J. Geophys. Res.*, *102*, 11,901–11,912, 1997.
- Rubin, A., Dikes vs. diapirs in viscoelastic rock, *Earth Planet. Sci. Lett.*, *119*, 641–659, 1993a.
- Rubin, A., On the thermal viability of dikes leaving magma chambers, *Geophys. Res. Lett.*, *20*, 257–260, 1993b.
- Rubin, A. M., Propagation of magma-filled cracks, *Annu. Rev. Earth Planet. Sci.*, *23*, 287–336, 1995.
- Rubin, A. M., Dike ascent in partially molten rock, *J. Geophys. Res.*, *103*, 20,901–20,919, 1998.
- Salters, V. J. M., and S. Hart, The Hf-paradox and the role of garnet in the MORB source, *Nature*, *342*, 420–422, 1989.
- Scott, D. R., and D. J. Stevenson, A self-consistent model for melting, magma migration and buoyancy-driven circulation beneath mid-ocean ridges, *J. Geophys. Res.*, *94*, 2973–2988, 1989.
- Secor, D. T., and D. D. Pollard, On the stability of open hydraulic fractures in the Earth's crust, *Geophys. Res. Lett.*, *2*, 510–513, 1975.
- Shaw, H. R., The fracture mechanisms of magma transport from the mantle to the surface, in *Physics of Magmatic Processes*, edited by R. B. Hargraves, pp. 201–264, Princeton Univ. Press, Princeton, N. J., 1980.
- Shaw, P. R., and J. Lin, Causes and consequences of variations in faulting style at the Mid-Atlantic Ridge, *J. Geophys. Res.*, *98*, 21,839–21,851, 1993.
- Shaw, W. T., and J. Lin, Models of oceanic ridge lithospheric deformation: Dependence on crustal thickness, spreading rate, and segmentation, *J. Geophys. Res.*, *101*, 17,977–17,993, 1996.
- Sleep, N. H., Tapping of magmas from ubiquitous mantle heterogeneities: An alternative to mantle plumes?, *J. Geophys. Res.*, *89*, 10,029–10,041, 1984.
- Sleep, N. H., Tapping of melt by veins and dikes, *J. Geophys. Res.*, *93*, 10,255–10,272, 1988.
- Small, C., Global systematics of mid-ocean ridge morphology, in *Faulting and Magmatism at Mid-ocean Ridges*, *Geophys. Monogr. Ser.*, vol. 106, edited by R. W. Buck et al., pp. 1–25, AGU, Washington, D. C., 1998.
- Sneddon, I. N., The distribution of stress in the neighborhood of a crack in an elastic solid, *Proc. R. Soc. London*, *187*, 229–260, 1946.
- Sotin, C., and E. M. Parmentier, Dynamical consequences of compositional and thermal density stratification beneath spreading centers, *Geophys. Res. Lett.*, *16*, 835–838, 1989.
- Sparks, D. W., and E. M. Parmentier, Melt extraction from the mantle beneath spreading centers, *Earth Planet. Sci. Lett.*, *105*, 368–377, 1991.
- Spence, D. A., and D. L. Turcotte, Magma-driven propagation of cracks, *J. Geophys. Res.*, *90*, 575–580, 1985.
- Spence, D. A., and D. L. Turcotte, Buoyancy-driven magma fracture: A mechanism for ascent through the lithosphere and emplacement of diamonds, *J. Geophys. Res.*, *95*, 5133–5139, 1990.
- Spence, D. A., P. W. Sharp, and D. L. Turcotte, Buoyancy-driven crack propagation: A mechanism for magma migration, *J. Fluid Mech.*, *174*, 135–153, 1987.
- Spiegelman, M., Physics of melt extraction: Theory, implications and applications, *Philos. Trans. R. Soc. London, Ser. A*, *342*, 23–41, 1993.
- Spiegelman, M., and T. Elliott, Consequences of melt transport for uranium series disequilibrium in young lavas, *Earth Planet. Sci. Lett.*, *118*, 1–20, 1993.
- Spiegelman, M., and D. McKenzie, Simple 2-D models for melt extraction at mid-ocean ridges and island arcs, *Earth Planet. Sci. Lett.*, *83*, 137–152, 1987.
- Spiegelman, M., P. B. Kelemen, and E. Aharonov, Causes and consequences of flow organization during melt transport: The reaction infiltration instability in compactable media, *J. Geophys. Res.*, *106*, 2061–2077, 2001.
- Stevenson, D. J., Spontaneous small-scale melt segregation in partial melts undergoing deformation, *Geophys. Res. Lett.*, *16*, 1067–1070, 1989.
- Tada, H., P. C. Paris, and G. R. Irwin, *The Stress Analysis of Cracks Handbook*, Dell Res. Corp., St. Louis, Mo., 1985.
- Takada, A., Experimental study on propagation of liquid-filled cracks in gelatin: Shape and velocity in hydrostatic stress condition, *J. Geophys. Res.*, *95*, 8471–8481, 1990.
- Takada, A., Accumulation of magma in space and time by crack interaction, in *Magmatic Systems*, edited by M. P. Ryan, pp. 241–257, Academic, San Diego, Calif., 1994a.
- Takada, A., Development of a subvolcanic structure by the interaction of liquid-filled cracks, *J. Volcanol. Geotherm. Res.*, *62*, 207–224, 1994b.
- Ten Brink, U., Volcano spacing and plate rigidity, *Geology*, *19*, 397–400, 1991.
- Thatcher, W., and D. P. Hill, A simple model for fault-generated morphology of slow spreading ridges, *J. Geophys. Res.*, *100*, 561–570, 1995.
- Toomey, D. R., W. S. D. Wilcock, S. C. Solomon, W. C. Hammond, and J. A. Orcutt, Mantle seismic structure beneath the MELT region of the East Pacific Rise from *P* and *S* wave tomography, *Science*, *280*, 1224–1226, 1998.
- Turcotte, D. L., and G. Schubert, *Geodynamics: Applications of Continuum Physics to Geological Problems*, John Wiley, New York, 1982.
- Webb, S., and D. W. Forsyth, Structure of the upper mantle under the EPR from waveform inversion of regional events, *Science*, *280*, 1227–1229, 1998.
- Weertman, J., Theory of water-filled crevasses in glaciers applied to vertical magma transport beneath oceanic ridges, *J. Geophys. Res.*, *76*, 1171–1183, 1971.
- Wessel, P., and W. H. F. Smith, New version of the Generic Mapping Tools released, *Eos Trans. AGU*, *76*, 329, 1995.
- Zimmerman, M. E., S. Zhang, D. L. Kohlstedt, and S. Karato, Melt distribution in mantle rocks deformed in shear, *Geophys. Res. Lett.*, *26*, 1505–1508, 1999.

G. Ito and S. J. Martel, Department of Geology and Geophysics, University of Hawaii at Manoa, 1680 East-West Road, Honolulu, HI 96822, USA. (gito@hawaii.edu; martel@soest.hawaii.edu)

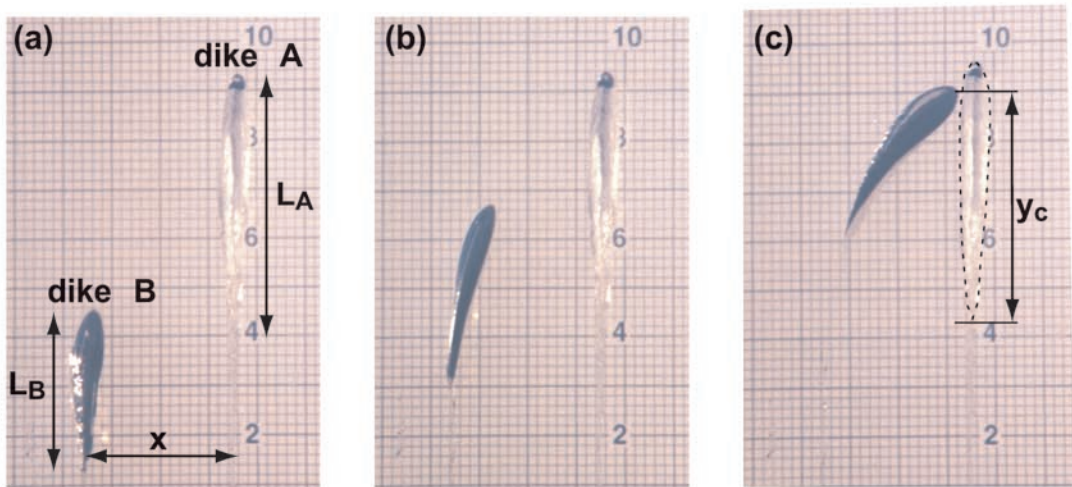


Figure 2. Time series of photographs illustrating how dike B (air) interacts with dike A (hexane). Dike tails are very thin so only dike heads are visible. (a) Both dikes are initiated parallel to each other. (b) As dike B ascends, it begins to curve toward dike A. (c) Dike B intersects dike A at a height y_c measured above the base of dike A. The head of dike A is outlined for clarity.